Chapter 1

Introduction and literature review

1.1 Introduction to the family of Hall effect

1.1.1 Ordinary Hall effect

When a conductor carrying an electric current is placed in the magnetic field; an electric field develops perpendicular to the plane of current and magnetic field directions [1, 2]. Let us consider a conductor carrying current I_x placed in a perpendicular magnetic field H_z as shown in Fig.1.1(a). Let's suppose the conduction is governed by the electron and the velocity of the electron is v_x, therefore, the Lorentz force acting on the electron can be given as

$$F = -e(v_x \times H_z) \tag{1.1}$$

In the equilibrium condition, the Lorentz force balances the transverse electric field, therefore

$$-e(v_x \times H_z) = -eE_y$$

$$E_y = v_x \times H_z$$

Since the direction of electric current is orthogonal to the applied magnetic field, hence

$$E_y = v_x H_z \tag{1.2}$$

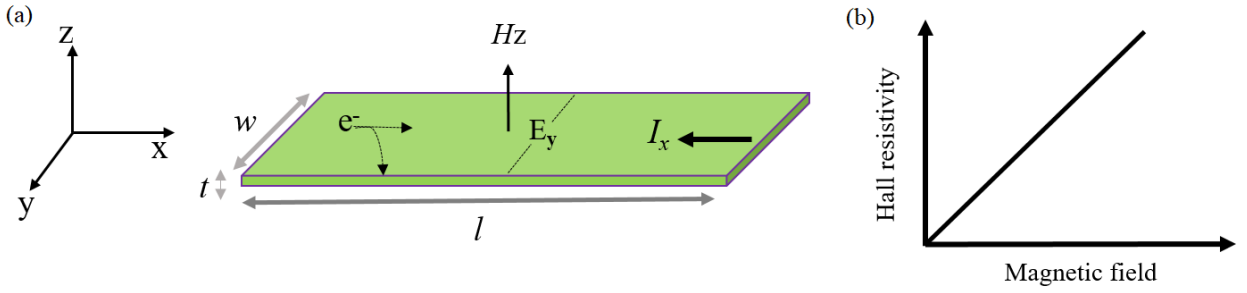

Figure 1.1: (a) Schematic diagram of Hall effect. (b) A typical Hall resistivity versus magnetic field curve.

For a conductor the current density (J_x) can be given as

$$J_x = nev_x \tag{1.3}$$

where n denotes the charge carrier density. From Eq.1.2 and Eq.1.3 together with using the relations J_x=$\frac{I_x}{w.t}$ and E_y=$\frac{V_y}{w}$,

$$\frac{1}{ne} = \frac{V_y t}{I_x H_z} = R_0 \tag{1.4}$$

Here R_0 is known as the normal (ordinary) Hall coefficient. The common unit of R_0 is m^3/C or ohm-cm/Oe. The Hall effect is a very versatile measurement technique to measure the carrier density and strength of a magnetic field. From Eq.1.4

$$R_{xy} = \frac{V_y}{I_x} \propto H_z$$

i.e. the Hall resistance varies linearly with the magnetic field. Fig.1.1 (b) shows a graphical diagram of the variation of Hall resistivity with an applied magnetic field. A schematic diagram of the Hall effect is also shown in Fig.1.3(a).

1.1.2 Anomalous Hall effect

One year later of the Hall effect discovery, E. Hall himself observed that the Hall effect becomes 10 times more pronounced in iron (Fe) in comparison to gold or silver. This phenomenon is known as anomalous Hall effect (AHE) [1, 2]. E. Hall further investigated AHE in the Nickel (Ni), and Cobalt (Co) and found that AHE increases steeply at low fields and saturates at the higher field region [3]. Kundt noted that the saturation of Hall resistivity in Fe, Ni, and Co exhibits a proportional relationship with the magnetization of the sample [4]. In 1929, Smith and Sears divided the Hall voltage in Permalloy into two parts: one related to magnetization intensity and the other to the material H-field [5]. Pugh and Lipper studied the Hall effect in the ferromagnetic material and concluded that the Hall voltage is a single-valued function of magnetization [6, 7]. Following Smit and Sears [5], and the careful high field measurement of the Hall effect on Ni, Pugh suggested that

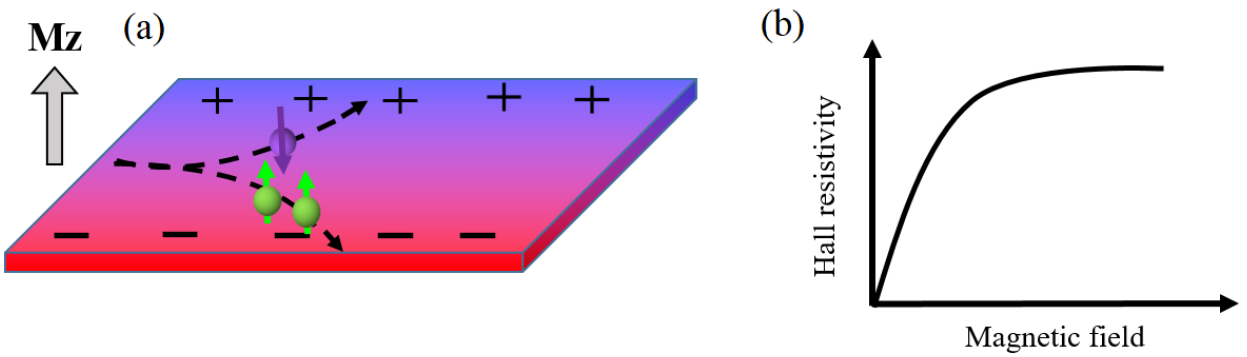

Figure 1.2: (a) Schematic diagram of anomalous Hall effect. (b) A typical Hall resistivity curve for ferromagnets.

the Hall resistivity in ferromagnetic materials can be written as [8]

$$\rho_{xy} = R_0 H_z + R_s M_z \tag{1.5}$$

where R_s is the anomalous Hall coefficient, which exceeds the ordinary Hall coefficient (R_0) for ferromagnetic materials by at least one or two orders of magnitude. Figure 1.2(a) shows a visual diagram of the AHE, where the spin-up and down electrons traverse in opposite directions. A graphical diagram of the Hall resistivity curve for the ferromagnetic material is shown in Fig. 1.2(b). The Hall resistivity curve deviates from its linear behavior with the magnetic field, unlike the ordinary Hall effect. Instead, it follows the typical magnetization curve of ferromagnets, suggesting that AHE goes beyond the classical Hall effect originated from Lorentz force [1]. A schematic diagram of AHE is also depicted in Fig. 1.3(b).

1.1.3 Spin Hall effect

The spin Hall effect (SHE) is a remarkable phenomenon in the physics of condensed matter, which elucidates the conversion of charge current into pure spin-current in non-magnetic materials facilitated by the spin-orbit interaction even in the absence of the magnetic field [9]. A schematic diagram of the SHE is shown in Fig. 1.3(c). The inverse SHE describes the conversion of pure spin-current into the charge current in the non-magnetic material through spin-orbit interactions. [9, 10]. The SHE occurs because of the spin and direction-dependency of the electron scattering due to the magnetic field of the spin-orbit interaction [11]. In a paramagnetic material, where there

is an equilibrium between up and down electrons, the SHE results in a null charge current, leading to the presence of a pure spin current [9]. M. I. Dyakonov and V. I. Perel first unveiled the SHE in 1971. The experimental validation was achieved much later in 2004 by Kato et al. through optical detection in the GaAs and $In_{0.07}Ga_{0.93}As$ [12]. Later the SHE was discovered in the materials with large spin-orbit coupling (SOC), which is necessary for the significant SHE [13–17]. The SHE is useful for spintronic devices such as spin transistors, diodes, and logic gates, with transformative potential in electronics [9]. It also enables magnetization control via spin-orbit torque, impacting magnetic memory and energy-efficient storage [9, 10].

1.1.4 Quantum Hall effect

The quantum Hall effect (QHE) represents a pioneering discovery in condensed matter physics that occurs in a two-dimensional electron system placed in a strong magnetic field and low temperatures near absolute zero [18]. A diagrammatic representation of the QHE is shown in Fig. 1.3(d). Discovered by Klaus von Klitzing in 1980, the QHE has revolutionized the understanding of the fundamental properties of electrons in a crystalline lattice and has essential implications for metrology and the study of topological states of matter [19]. The hallmark of the QHE is the quantization of the Hall resistance (R_H) to exceptionally precise values that are integer multiples of a fundamental constant $\frac{h}{e^2}$ =25.812 kΩ, where 'e' represents the electron charge and 'h' denotes the Planck constant. The QHE arises due to the formation of the Landau levels at the strong magnetic field. The quantized Hall resistance is independent of the sample geometry suggesting the topologically protected chiral edge or surface states of the system. These electrons move without scattering, leading to a dissipationless current, holding promise for electronic device applications [20]. The detailed discussion of the QHE is presented in the section 1.3.1.

1.1.5 Quantum spin Hall effect

The QHE requires the time-reversal ($\mathcal{T}$) symmetry breaking due to the external magnetic field [18]. In insulators with a suitable band structure, edge channel transport can also happen without an external magnetic field. In this scenario, edge states emerge, with electrons of opposite spins moving in opposite directions—a phenomenon termed the quantum spin Hall (QSH) effect [Fig. 1.3(e)] [22].

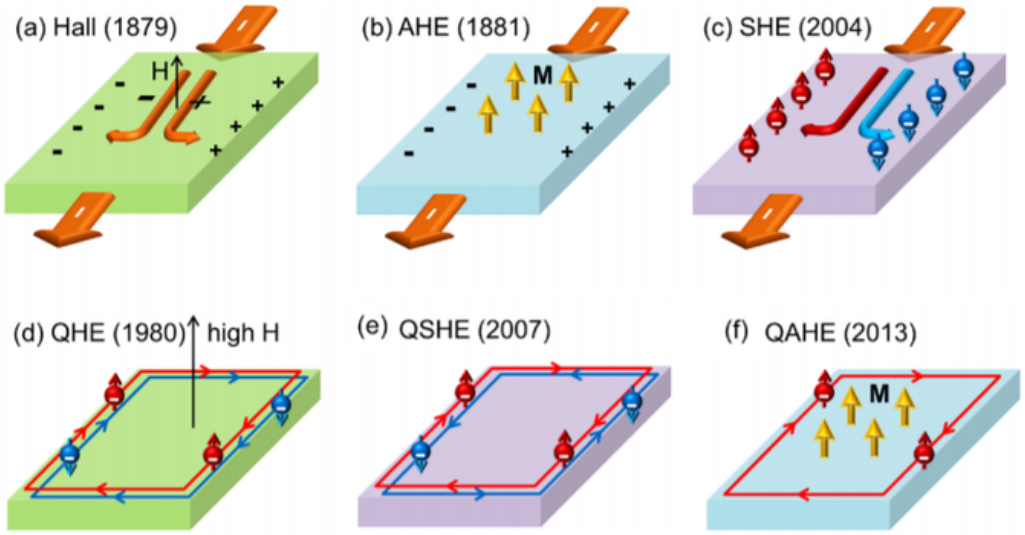

Figure 1.3: The schematic diagram of the family of Hall effect [21].

This leads to the quantized spin Hall conductivity in the unit of $2\,\frac{e^2}{h}$. The existence of the QSH effect was theoretically proposed by Bernevig and S.C. Zhang in 2006, where they predicted the formation of the landau level through the velocity-dependent force arising from the strain which is equivalence to the SOC [22]. In the same year, they also proposed that the QSH state could exist in semiconductor quantum wells made of mercury telluride and cadmium telluride. Varying quantum well thickness, the topological phase transition from the normal state to the QSH insulator state occurs at the critical thickness of 64 Å [22]. This prediction has been experimentally verified in an experiment performed in the Molenkamp labs at Würzburg in Germany [23].

1.1.6 Quantum anomalous Hall effect

The broken $\mathcal{T}$-symmetry can induce AHE in the ferromagnetic materials [1]. The quantized version of AHE is termed as quantum anomalous Hall (QAH) effect [24]. A visual diagram of the QAH effect is depicted in Fig. 1.3(f). The QHE requires a strong magnetic field for the quantized Hall conductance, the question arises naturally whether this quantization is possible without the external magnetic field. The answer, fortunately, is yes. The 2D topological insulators with broken $\mathcal{T}$-symmetry can give the QHE without an external magnetic field [25]. The first experimental evidence of the nearly accurate QAH effect was realized in the Cr and V-doped Bi_2Se_3 [26]. The magnetically doped elements break the $\mathcal{T}$-symmetry and combining with the SOC produces topo-

logically non-trivial chern bands. The realization of the QAH effect due to magnetic doping is difficult, due to the inhomogeneous distribution of the magnetic dopant. Therefore, a search for the intrinsic magnetic topological insulator is required. Recently, the QAH effect has been observed in the intrinsic magnetic topological insulator $MnBi_2Te_4$, attributed to the net magnetization resulting from the arrangement of an odd number of layers [27]. The QAH effect was also observed in the twisted bilayer graphene aligned with the hexagonal boron nitride due to the strong electron correlation, which polarizes the electron in a single spin and valley resolved moiré miniband [28].

1.1.7 Anomalous Nernst effect

The anomalous Nernst effect (ANE) is the thermoelectric counterpart of AHE, which utilizes the temperature gradient as an external field instead of the electric field [29]. In essence, both the AHE and ANE share a common conceptual foundation—namely, the generation of a transverse voltage in ferromagnetic materials. Compared to the Seebeck effect, it offers several advantages when applied to high-efficiency energy-harvesting devices. These advantages include a simpler lateral structure, increased flexibility, and significantly reduced production costs [29]. The ANE has profound implications for the emerging field of spintronics, offering novel avenues for the manipulation of electron spins and their associated degrees of freedom [29–31].

1.1.8 Topological Hall effect

In magnetotransport measurements of the magnetic materials, there is an instance when an additional Hall resistivity arises in addition to the ordinary and the anomalous Hall resistivity due to the interaction between the conduction electron and the non-trivial spin texture. This phenomenon is called the topological Hall effect (THE) [32–35]. In this context, the term non-trivial spin texture refers to spin arrangements that deviate from the conventional ferromagnetic or antiferromagnetic ordering, exhibiting a more complex and unconventional pattern of distribution. These types of spin textures are topologically stable means they can not be destroyed by continuous deformation of the field [36]. Due to the strong exchange coupling between the conduction electron and non-trivial spin structure, the conduction electron adiabatically follows the spins of texture thus picks up a real space Berry curvature, and traverses along the transverse direction [32]. Before the term THE is in-

troduced, the theory of non-zero scalar spin-chirality $\vec{S_i}\cdot(\vec{S_j}\times\vec{S_k})$ of spins was formulated to explain an additional term in Hall resistivity [37]. The scalar spin chirality produces the fictitious magnetic field according to the Berry phase mechanism. In 2004, P. Bruno *et al.* introduced the term 'THE' to distinguish this effect from the other related mechanisms [38]. The fictitious magnetic field due to scalar chirality is given as follows

$$b^z = \sum_{ijk} \vec{S_i} \cdot (\vec{S_j} \times \vec{S_k}) \hat{n}_{ijk}$$

where $\hat{n}_{ijk}$ represents a unit vector that is perpendicular to the triangle plane defined by the three sites i, j, and k. The additional Hall signal due to the scalar spin chirality was found in several systems such as $Nd_2Mo_2O_7$, where spins are at the kagome lattice [39, 40] and spin glass of AuFe due to the conical spin structure [41]. In 2009, Tony Skyrme discovered an intriguing spin structure called skyrmions, which exists alongside the non-coplanar spin structure in certain materials [42, 43]. Skyrmions are nanodomain spin structures with topological protection, where the spins wrap around a sphere and behave as solitons. This means skyrmions resist deformation through continuous changes in the field configuration [42]. Skyrmions have shown promise for applications in spintronic devices because they can be driven by very low current density [44]. In a skyrmion, the core electron's magnetic moment aligns antiparallel to the applied magnetic field, whereas at the periphery, it aligns parallel [45]. Moving from the periphery towards the core, the moment rotates between 0 and π degrees concerning the z-axis and completes a full 0 to 2π degree circular rotation [42]. In the case of Bloch-type skyrmions, the moment rotates perpendicular to the radial plane, whereas for Neel skyrmions, the moment rotates along the radial plane [42]. Additionally, antiskyrmions have been observed in the D_{2d} crystal lattice, which consists of both Bloch and Neel types of magnetization dynamics [46]. Helicity (γ) denotes the angle between the in-plane component of the magnetization and the radial direction [42]. Therefore the (γ) for Bloch type of skyrmions will be $\pm\pi/2$ and for Neel skyrmion this value will be zero [42]. The Bloch, Neel, and antiskyrmion are shown in Fig. 1.4 (a)-(c), respectively. The skyrmion can be indeed defined by the topological number/charge, which measures the binding number of normalized magnetization.

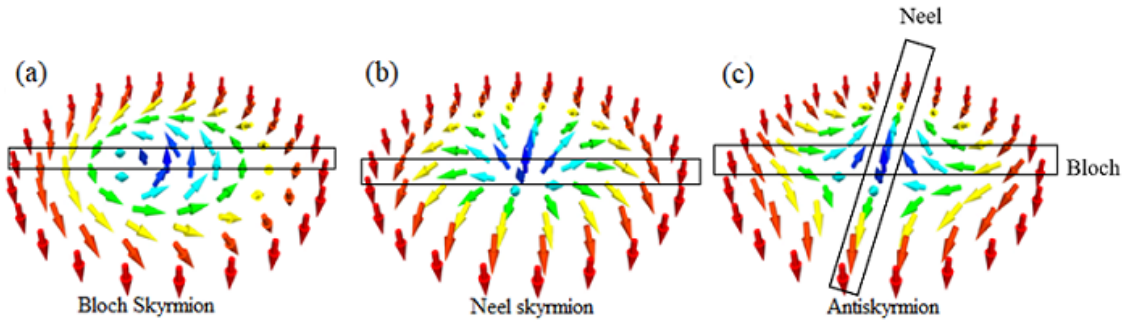

Figure 1.4: (a) Bloch Skyrmion. (b) Neel Skyrmion. (c) Antiskyrmion. [49]

In two dimensions the topological number of skyrmions is [47]

$$Q = \frac{1}{4\pi} \int \vec{m}.\left(\partial_x \vec{m} \times \partial_y \vec{m}\right) dx\, dy = \pm 1, \tag{1.6}$$

The normalized magnetization *m* wraps a sphere for the skyrmion and is thus quantized [47]. This non-trivial topology gives topological protection to the spin texture and hence it can not be transformed continuously into another state different from Q e.g. ferromagnetic state [36]. The magnetic skyrmions possess a crucial solitonic nature, enabling particle-like movement, interactions, and excitations and these dynamic behaviors hold great potential for device applications [48]. Initially, skyrmions were discovered in the single crystal of non-centrosymmetric materials stabilized by the Dzyaloshinskii-Moriya interaction (DMI) [47, 50, 51]. The DMI arises in systems lacking inversion symmetry in the presence of SOC [52]. It is an antisymmetric exchange interaction acting between two neighboring spins, $\vec{S_i}$, and $\vec{S_j}$, and its Hamiltonian is given by $H_{DMI} = \vec{D} \cdot (\vec{S_i} \times \vec{S_j})$, where $\vec{D}$ represents the strength of the DMI [52]. The DMI favors the canting of the magnetic moment, and the type of the skyrmion formation depends on how the inversion symmetry is broken [42]. The inaugural material in this class was MnSi, its skyrmion phase was confirmed by temperature (T)-magnetic field (B) phase in the Neutron diffraction measurement [53]. Furthermore, in the $Fe_{1-x}Co_xSi$, the Lorentz transmission electron microscopy reveals the first time real-space observation of skyrmions [54]. With the application of a magnetic field (50-70 mT) to the thin film of $Fe_{0.5}Co_{0.5}Si$, a hexagonal pattern of swirling spin textures revealed the presence of skyrmions. The skyrmion in non-centrosymmetric systems has been observed in several materials such as $Mn_{1-x}Fe_xGe$ [55], FeGe [56, 57], Cu_2OSeO_3 [58, 59], and $Co_8Zn_8Mn_4$ [60], etc. Subse-

quently, skyrmion was detected in the magnetic thin films deposited on heavy metal substrates, due to the significant DMI originating from the disruption of inversion symmetry at the interface. The Fe monolayer and bilayer of PdFe on Ir(111) was the first discovered material in this class, where substantial DMI was observed at the Fe/Ir(111) interface [43]. During the quest for skyrmions, it was discovered that even centrosymmetric material can stabilize the skyrmion bubbles, despite zero DMI [61, 62]. In contrast to DMI-stabilized skyrmions, which have a fixed chirality, centrosymmetric skyrmion bubbles exhibit two degrees of freedom; helicity and vorticity, and hence the chirality can be altered through external stimuli [63, 64]. Skyrmion bubbles are classified topologically in the same way as the Bloch skyrmions in the B20 magnets and therefore said to be the 'dipolar skyrmions' or simply 'skyrmions' [65]. A route to the formation of a skyrmion in centrosymmetric material is magnetic frustration, particularly geometric frustration where the competing interaction among the localized spins can not simultaneously satisfy due to the lattice geometry, leading to the highly degenerate ground state e.g. the non-trivial modulated spin-order, spin liquid, etc [42]. In the triangular lattice, characterized by Heisenberg spins (instead of Ising spins), and incorporating second (or third) neighbor exchange interactions, theoretical studies demonstrate the emergence of multiple-q states when the magnetic field is applied perpendicular to the 2D plane and one of these states is the skyrmionic state, which qualifies as a triple-q state [66]. This magnetic frustration phenomenon is also encountered in itinerant magnets that involve the interaction between local spins and conduction electrons (Ruderman-Kittel-Kasuya-Yosida (RKKY)) present on the Fermi surface [67]. On lattices exhibiting high symmetry, the RKKY interaction can result in helical spin textures along with multiple q states, among which the skyrmions are the notable example [68, 69]. Gd_2PdSi_3 [68], $Gd_3Ru_4Al_{12}$ [69], and $GdRu_2Si_2$ [70] and $SrFeO_3$ [71] are prime examples of centrosymmetric systems that unveiled skyrmion states due to the magnetic frustration and higher-order exchange interactions. The skyrmion in centrosymmetric systems can also emerge from competing magnetic interactions such as exchange interaction, magnetic anisotropy, and long-range dipolar interactions. For example, NiMnGa [72], Ni_2MnGa [73], $(Mn_{1-x}Ni_x)_{65}Ga_{35}$ [64], Fe_3Sn_2 [74, 75], Mn_4Ga_2Sn [62], $La_{(1-x)}Sr_xMnO_3$ [45], Fe_3GeTe_2 [63] are reported to exhibit skyrmionic structure due to the competing magnetic interaction.

1.2 Origin of anomalous Hall effect

In the initial age of AHE research, the microscopic origin of AHE was not well understood and was the subject of controversy. The magnetization of the ferromagnetic materials is involved in the AHE [1], which suggests that SOC plays a significant role in AHE. SOC is the relativistic effect experienced by an electron (magnetic field of spin-orbit interaction created by the electric field of localized electron or magnetic impurity in the rest frame of the electron) in the crystal lattice and introduces a correlation between the electron spin and its momentum [76]. The SOC can be understood by considering that the magnetic field exerts a force on the electron's charge, while the SOC specifically affects the electron spin [77]. The presence of SOC induces a magnetic field that leads to direction-dependent scattering of conduction electron spins [78]. Consequently, the AHE manifests itself in materials exhibiting an imbalance between the number of spin-up and spin-down electrons. The microscopic origin of AHE includes two classes of mechanisms, namely extrinsic and intrinsic mechanisms. The extrinsic mechanism results from electron scattering by spin-orbit-coupled impurities, whereas the intrinsic mechanism does not depend on scattering and relies exclusively on the Berry curvature linked with the band structure of the system [79].

1.2.1 Extrinsic mechanism

The extrinsic mechanism of AHE is related to the scattering of the spin-polarized electron by spin-orbit coupled magnetic impurities in the crystal [1]. These impurities possess a potential that distinguishes between spin-up and spin-down electrons, causing them to scatter in different transverse directions [1, 79]. As a consequence, the AHE manifests in the materials. It has been observed that extrinsic AHE does not exist in the perfect lattice and is finite for the disorder metal at a finite temperature suggesting that it is closely related to the resistivity of materials [80]. J. Smit conducted a study on the AHE measurement of both a pure Ni sample and a Ni-Fe-Cu alloy. The results indicated that while the pure Ni exhibited zero AHE as it approached T=0 K, the disordered Ni alloy showed a finite AHE at temperatures near T=0 K [80]. These findings imply that impurities have a significant impact on the AHE of ferromagnetic materials. Extrinsic mechanisms include two types of scattering namely skew scattering and side jump. Skew scattering occurs due to the dif-

ferent scattering probabilities of electrons in opposing transverse directions- a phenomenon arises when scattering potential includes an antisymmetric part of the Hamiltonian [81]. The scattering of conduction electrons is skewed only when the matrix element of scattering potential between the state of $\vec{k}$ and $\vec{k'}$ are changed by the interchange of $\vec{k}$ and $\vec{k'}$ *i.e.* the transition probability from $\vec{k}$ to $\vec{k'}$ is not equal to that from $\vec{k'}$ to $\vec{k}$. The Hamiltonian suggested by Kondo for the interaction of conduction electron with the localized moment is given as [81, 82]

$$H_{cl} = -1/N \sum a^*_{\vec{k'}} a_{\vec{k}} (g-1)\Gamma(|\vec{k}-\vec{k'}|)\vec{J}\cdot\vec{S} + \frac{i}{2}(2-g)\times F_2 \vec{J}\cdot(\vec{k}\times\vec{k'}) + 2id_2F_3[\vec{J}\cdot(\vec{k}\times\vec{k'})](\vec{J}\cdot\vec{S}) \quad (1.7)$$

Here $a_{\vec{k}}$ is the destruction operator of wave vector $\vec{k}$. The terms N, g, J, and S represent the total number of atoms in the crystal, gyromagnetic ratio, total angular momentum, and spin angular momentum, respectively. The first term of Eq.1.7 is a simple spin-spin interaction and the second term contains $\vec{k}\times\vec{k'}$ in the first order, which is an antisymmetric term that gives rise to the skew scattering. The material with 4f moment exhibits the non-zero value of orbital and spin angular momentum, therefore, the Coulomb interaction involving the conduction electron and 4f electrons comprises contributions from both spin and orbital exchange terms $\sim$ (2-g)$\vec{l}\cdot\vec{J}$, where g is the gyromagnetic ratio and $\vec{J}$ is total angular momenta of 4f electrons [81]. This orbital exchange term has an antisymmetric character due to an odd value of l, resulting the skew scattering. From Eq.1.7 it is clear that the skew scattering term vanishes for g=2, as for Gd a paramagnetic material, however, the experiments suggest that skew scattering is large for Gd doped in Ag or Au [81]. Therefore, there should be a second mechanism, which does not arise from the asymmetry of H_{cl}. The skew scattering term can exist by the scattering of conduction electrons with localized non-magnetic $5d$ electrons of Gd when considering the spin-orbit coupling of $5d$ electrons *i.e.* $\vec{l}\cdot\vec{s}$ interaction of impurity potential giving an effectively $\vec{l}\cdot\vec{J}$ interaction similar to the orbit exchange. The $5d$ virtual bound state results in a strong scattering of a partial wave with l=2. When SOC has included the degeneracy of states J=5/2 and J=3/2 is raised and the virtual band state is split into two centers at $E_{5/2}$ and $E_{3/2}$ with different densities of states, which results in different phase shift of partial wave (as the phase shift depends on the no. of scatter *i.e.* impurities) [1]. Electrons with a z-component

of angular momentum (say m) favor leftward scattering due to strong hybridization with virtual bound states other than one with -m. When the spin-up electron density is less than half-filled, it flips the direction of the AHE [1]. The skew scattering caused by magnetic impurities of transition metals is linked to the presence of local orbital moments and involves orbital exchange between conduction and localized electrons. Also, the contribution of spin-orbit interactions exists in some metals with d orbitals of the conduction band. The skew scattering depends upon the number of scatter present in the material [80]. The Hall resistivity (ρ_{xy}) arising from skew scattering exhibits a proportionality to the longitudinal resistivity (ρ_{xx}) and dominant usually at low temperatures [81]. A schematic diagram of skew scattering is depicted in Fig.1.5(a).

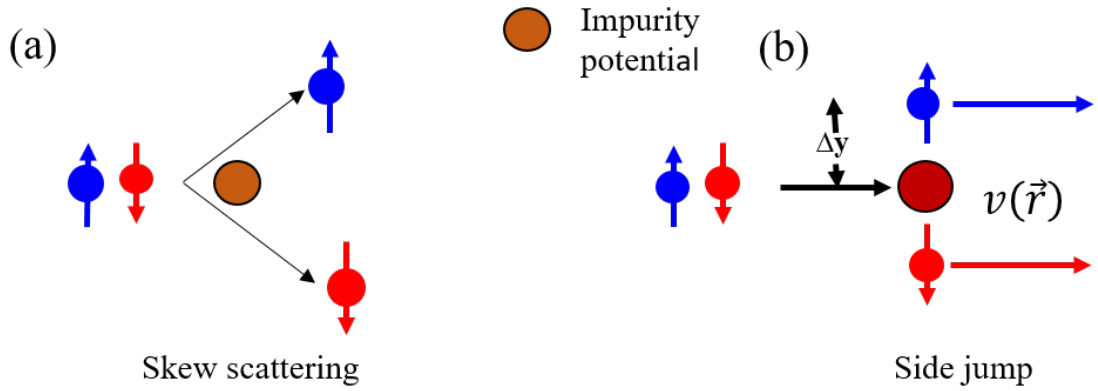

Figure 1.5: Schematic diagram of (a) skew scattering and (b) side jump.

The Hall resistivity is influenced by another mechanism, which was discovered during experiments with Fe-dilute alloys, where the variation of R_s with ${\rho_{xx}}^2$ cannot be explained by the skew scattering mechanism [83, 84]. This contribution appears when $\frac{\hbar}{E_f \tau}$ is not small *i.e.* for the high temperature or concentrated alloys. Berger proposed this mechanism as a side jump Δy, where a transverse displacement of the wave packet of an electron occurs when scattering from the impurity or phonon [84]. In the realm of quantum mechanics, a free electron is treated as a wave packet that propagates with an average group velocity in a linear trajectory. Suppose that an electron, after scattering with a spin-orbit-coupled impurity, follows a trajectory where the incident and scattered paths no longer intersect at the center of the scattering potential. In this case, a slight and sudden lateral displacement Δy occurs, as illustrated in Fig. 1.5(b). Skew scattering finds its explanation within the framework of the classical Boltzmann equation, whereas the side jump phenomenon is nonclassical. The side

jump mechanism can explained through considerations of localized electrons or wave packets [84]. This side jump results from the distortion of wave function locally due to the scattering potential, which induces the local current density. In addition to the displacement in the transverse direction to the incident $\vec{k}$, a longitudinal displacement Δx also exists, but it has no impact on the Hall effect. In a weak and short-range scattering potential, the side jump can be given as [84]

$$\Delta y = \frac{1}{6} k_0 \lambda_c^2 \tag{1.8}$$

where $\lambda_c = \hbar/mc$ is rationalized Compton wavelength. For the bands electron the $\Delta y \sim 10^{-11}$ m. It is worthwhile to note here that the Δy is independent of the strength and radius of scattering potential [1, 84].

1.2.2 Intrinsic mechanism

The intrinsic mechanism was first postulated by Karplus and Luttinger (K-L), which is the first theory fully based on the Bloch wave function [85]. K-L suggested that the intrinsic mechanism is a consequence of the SOC on the magnetic electrons [85]. The Hamiltonian of SOC is given as [85]

$$H = \frac{1}{4m^2c^2} \frac{(\vec{M} \times \vec{\boldsymbol{\nabla}} \vec{V}) \cdot \vec{p}}{M_s} \tag{1.9}$$

The SOC introduces the left-right asymmetry in the stationary state of the system and when an electric field is applied, a current flows through perpendicular to both the electric field and the magnetization. K-L theory neglected all types of disorder and hence was based on fully intrinsic mechanism. The anomalous velocity due to SOC found by K-L is as follows [1]

$$\vec{v} = -\frac{e}{m\Delta^2} \sum_{kn} \rho_0(\epsilon_{nk}) [\vec{E} \cdot \vec{v_{nk}}] \vec{F_{nk}} \tag{1.10}$$

where ϵ_{nk} represents energy of the Bloch state, Δ represents the mean interband energy separation and $\vec{F_{nk}}$ corresponds to the force $i \langle n\vec{k}|[H_{SOI}, \vec{p}]|n\vec{k}\rangle$. The calculated R_s by K-L is as follows [1, 85]

$$R_s = \frac{2e^2 H_{so}}{m\Delta^2} \delta(\frac{m}{m^*}) \rho_{xx}^2 \tag{1.11}$$

The ρ_{xx}^2 dependency of R_s, suggests that the off-diagonal conductivity σ_H is unaffected by the transport lifetime τ, a deviation from the behavior observed for diagonal conductivity σ. The anomalous velocity of electrons is subsequently derived from the solution of the semiclassical Boltzmann equation in a weak perturbative electric field, which gives an additional term in the equation of motion, called the Berry curvature term which induces the anomalous velocity to the electrons [86–88]. According to quantum mechanics, when an electron undergoes adiabatic perturbation, it returns to its original quantum state with a phase factor [89]. The concept is simple; the vector potential of a small DC field ($\vec{E}$= -$\delta\vec{A}/\delta$t) increases with the time due to which each Bloch state goes through the adiabatic evolution under this vector potential and acquires the additional phase [90]. Let's consider a system defined by Hamiltonian H, which depends on time (t) through a parameter space $\boldsymbol{R}$;

$$H = H(\boldsymbol{R}), \boldsymbol{R} = \boldsymbol{R}(t)$$

Here we are interested in the situation, where the $\boldsymbol{R}(t)$ changes slowly with time along a path C. The natural basis consists of eigen state $|n(\boldsymbol{R})\rangle$ of H($\boldsymbol{R}$) that follows

$$H(\boldsymbol{R})|n(\boldsymbol{R})\rangle = E_n|n(\boldsymbol{R})\rangle \tag{1.12}$$

Eq.1.12 gives $\boldsymbol{R}$-dependent phase factor of $|n(\boldsymbol{R})\rangle$, which can be removed by assuming the continuity (smoothness) and uniqueness of the phase of the basis function along path C. Any adiabatic eigenstate $|n(\boldsymbol{R}(0))\rangle$ evolves with Hamiltonian H and after time t the wave function of Bloch wave can be written as

$$|\psi_n(t)\rangle = e^{i\gamma_n t} exp\left[\frac{-i}{\hbar}\int_0^t dt' \epsilon_n(\boldsymbol{R}(t'))\right]|n(\boldsymbol{R}(t))\rangle \tag{1.13}$$

Here second exponential term is known as the dynamical phase factor. The solution of the Schrodinger equation

$$i\hbar\frac{\partial|\psi_n(t)\rangle}{\partial t} = H|\psi_n(t)\rangle$$

for the state in 1.13 gives phase factor γ_n as [90]

$$\gamma_n = \int_c A_n(\boldsymbol{R}) \cdot d\boldsymbol{R} \tag{1.14}$$

where $\mathrm{A}_n(\boldsymbol{R})$ is the Berry connection defined as

$$|A_n(\boldsymbol{R})\rangle = i\langle n(\boldsymbol{R})|\frac{\partial}{\partial \boldsymbol{R}}|n(\boldsymbol{R})\rangle \tag{1.15}$$

$|A_n(\boldsymbol{R})\rangle$ is a gauge-dependent quantity. If we choose some arbitrary smooth function $\xi(\boldsymbol{R})$ such that $\mathrm{A}_n(\boldsymbol{R})$ transform as $\mathrm{A}_n(\boldsymbol{R})$-$\frac{\partial}{\partial \boldsymbol{R}}\xi\,(\boldsymbol{R})$, it is quite possible to make $\gamma_n = 0$ for this smooth arbitrary function, hence the Eq.1.13 leaves only with a dynamical phase factor. This is the reason why γ_n has long been deemed neglected until Berry imposed a condition on path C that it should be closed path to realizing the γ_n as a physical observable. In the cyclic evolution, γ_n undergoes changes only in the multiple of 2π under the gauge transformation, and γ_n now termed as Berry phase represented as

$$\gamma_n = \oint_c A_n(\boldsymbol{R}) \cdot d\boldsymbol{R} \tag{1.16}$$

Berry phase is geometrical and is written in line integral along a closed loop. It is independent of the precise rate of change along the loop, giving freedom to represent it in terms of any local geometrical quantity. Hence, the Berry phase can be represented in relation to the integral of the Berry curvature across the region enclosed by the closed path. Following Stokes theorem, the γ_n can be written as

$$\gamma_n = \oint_s d\mathbf{S} \cdot \Omega_n(\boldsymbol{R}) \tag{1.17}$$

where

$$\Omega_n(\boldsymbol{R}) = \nabla_R \times A_n(\boldsymbol{R}) \tag{1.18}$$

Equation 1.18 is analogous to the $\vec{B} = \vec{\nabla} \times \vec{A}$ of classical electrodynamics suggesting that $\Omega_n(\mathbf{R})$ acts as the magnetic field in the reciprocal space. The Berry curvature component in the two-dimension

plane of ij component can be written as [90]

$$\Omega_{ij}^{n} = \frac{\partial}{\partial R_i} A_j(\boldsymbol{R}) - \frac{\partial}{\partial R_j} A_i(\boldsymbol{R})$$

$$= i\langle \frac{\partial}{\partial R_i} u_n(\boldsymbol{R}) | \frac{\partial}{\partial R_j} u_n(\boldsymbol{R}) \rangle - i\langle \frac{\partial}{\partial R_j} u_n(\boldsymbol{R}) | \frac{\partial}{\partial R_i} u_n(\boldsymbol{R}) \rangle \tag{1.19}$$

It is rather complicated to evaluate the Berry curvature in real crystal using Eq.1.19 due to the involvement of the derivative of the wave function, which can be evaluated under any gauge choice. The alternate equation to calculate the Berry curvature in the real system is as follows [91]

$$\Omega_{ij}^{n} = i \sum_{n \neq m} \frac{\langle u_n | \frac{\partial H}{\partial R^i} | u_m \rangle \langle u_m | \frac{\partial H}{\partial R^j} | u_n \rangle - (i \leftrightarrow j)}{(E_n - E_m)^2} \tag{1.20}$$

which requires only eigenfunction that can be supplied from first principle calculations. For the crystal lattice, the band structure offers an avenue to study the Berry phase effect as the Brillouin zone serves as parameter space. For the independent electron approximation, the Hamiltion of an electron depends on its kinetic energy and the periodic potential of the lattice. The wave vector $\boldsymbol{q}$ dependent Hamiltonian requires an external field such as an electric field. The $\boldsymbol{q}$ dependent eigenstate *i.e.* $|u_n(\boldsymbol{q})\rangle$ serves as basis function of Hamiltonian H($\boldsymbol{q}$) and hence electron pickup a Berry phase

$$\gamma_n = \oint_c d\boldsymbol{q} \cdot \langle u_n(\boldsymbol{q}) | i\nabla_q | u_n(\boldsymbol{q}) \rangle$$

where C must be a closed path either application of magnetic field or the electric field so that $\boldsymbol{q}$ swaps the entire Brillouin zone. The corresponding Berry curvature in a crystal lattice can be written as

$$\Omega_n(\boldsymbol{q}) = \nabla_q \times \langle u_n(\boldsymbol{q}) | i\nabla_q | u_n(\boldsymbol{q}) \rangle \tag{1.21}$$

From Eq.1.21, it is evident that the Berry curvature is the intrinsic property of the system which only depends on the wavefunction. In the $\boldsymbol{q}$ space the $\Omega_n(\boldsymbol{q})$ follows the symmetry constraint (i) preserving $\mathcal{T}$-symmetry, *i.e.* $\Omega_n(-\boldsymbol{q})$ = -$\Omega_n(\boldsymbol{q})$ (ii) preserving $\mathcal{P}$-symmetry *i.e.* $\Omega_n(-\boldsymbol{q}) = \Omega_n(\boldsymbol{q})$. This implies that when a system exhibits both $\mathcal{T}$ and $\mathcal{P}$ symmetries at the same time, the Berry

curvature is zero. Hence, to attain a nonzero Berry curvature, the material must exhibit either a nonzero electric polarization, disrupting $\mathcal{P}$-symmetry, or spontaneous magnetization, breaking $\mathcal{T}$-symmetry [90]. Based on the semiclassical Boltzmann equation the anomalous Hall conductivity (AHC) can be derived by calculating the current density due to the application of uniform external fields and given by [91]

$$\sigma_{ij} = -\frac{e^2}{\hbar}\sum_n \int \frac{d^3k}{(2\pi)^3}\Omega_{ij}^n f_n. \tag{1.22}$$

where f_n is the Fermi distribution function.

1.2.3 Scaling relation and progress in anomalous Hall effect

A universal scaling [92] suggests that the origin of AHE can be divided into three broader regimes depending on the conductivity of materials. In the clean regime with high conductivity ($\sigma_{xx} > 10^6$ S/cm), the AHE arises from the skew scattering mechanism and the scaling relation follows $\rho_{xy} \propto \rho_{xx}$ or $\sigma_{xy} \propto \sigma_{xx}$. In the moderate regime or good metal regime (10^4 S/cm $< \sigma_{xx} < 10^6$ S/cm), the intrinsic mechanism dominates and the scaling relation follows $\rho_{xy} \propto {\rho_{xx}}^2$ or σ_{xy} is constant. In the bad metal regime ($\sigma_{xx} < 10^4$ S/cm), the contribution of the intrinsic mechanism becomes less and the scaling relation follows $\sigma_{xy} \propto {\sigma_{xx}}^{1.6}$. E. Hall first experimentally observed the AHE in 1881 although he could not explain the origin of AHE [1]. Kundt observed that the saturation of Hall resistivity in Fe, Ni, and Co is nearly proportional to the magnetization of the sample [4]. Following the discovery of three mechanisms explaining the origin of AHE, researchers began to unravel the connection between ρ_{xy} and ρ_{xx}. Karplus found the scaling relation $R_s \propto {\rho_{xx}}^{1.94}$ in the Fe [85], which validates the intrinsic mechanism. For cobalt the scaling relation $\rho_{AH} = a\rho_{xx} + b{\rho_{xx}}^2$ works well, which suggests multiple mechanism coexistence in the material [93]. A. Fert. found the linear relation between ρ_{xy} and ρ_{xx} in the Ni at low temperatures, which gives the skew scattering contribution of AHE [94]. Since the skew scattering and side jump have linear and quadratic dependence of anomalous Hall resistivity, the extrinsic mechanism was accepted to be responsible for AHE, and the intrinsic mechanism was ignored for a long time till the discovery of the Berry phase mechanism. The first principle calculation of the intrinsic AHE of bcc Fe gives the intrinsic AHC about 751 S/cm at zero temperature and 734 S/cm at room temperature, which is close to the experimental value [95, 96]. The angular value of calculated intrinsic AHC in Co

about 226 S/cm is close to the measured value of 205 S/cm [97]. Recently, Shukla *et al.* studied AHE in Co_2FeGe Heusler compound and found the experimental intrinsic AHC of about 78.6 S/cm, which is in good agreement with theoretically calculated AHC of about 77.29 S/cm [98]. Tian et al. proposed the scaling relation for the thin film of Fe [99]

$$\rho_{AH} = (\alpha\rho_{xx0} + \beta{\rho_{xx0}}^2) + b{\rho_{xx}}^2$$

or in the conductivity form

$$\sigma_{AH} = -(\alpha{\sigma_{xx0}}^{-1} + \beta{\sigma_{xx0}}^{-2}) - b$$

Here ρ_{xx0} is the residual resistivity and parameter b is the intrinsic AHC. α and β are the skew scattering and side jump parameters. They neglected the contribution of phonon in skew scattering, which works well for thin films of Fe. The intrinsic AHC was computed using the aforementioned equation across various thicknesses of Fe films. Remarkably, the intrinsic AHC for all the films converges to a consistent value of 1100 S/cm [99]. Recently, the effect of the disorder on the intrinsic AHC has been investigated. Sakuraba et.al. found that the improved anomalous Nernst conductivity in the $Co_2MnAl_{1-x}Si_x$ on improving the atomic ordering within the system [100]. Mende *et al.* found the experimental intrinsic AHC in the Fe_2-based Heusler alloys that lie between the calculated AHC for the full Heusler structure and the inverse Heusler structure [101]. The presence of antisite disorder in the alloys enhances the number of mirror symmetry planes when compared to the inverse Heusler structure, leading to an AHC that exceeds the calculated value for the inverse Heusler structure. Shahi *et al.* studied the effect of antisite disorder in Mn_2CoAl Heusler compound, where they found that the 25% disorder between Mn and Al sites increases the value of intrinsic AHC that is consistent with the experiment [102]. A study on Co_2FeAl also suggests that the antisite disorder increases the intrinsic AHC [103].

1.3 Topological materials

Topology originally is a mathematical discipline that investigates the characteristics of spaces that remain unchanged under continuous deformation [104–106]. The continuous deformation implies

that neighboring points on the object maintain their proximity, and there are no operations involving cutting and rejoining [104]. For example, in Fig.1.6 (a), the circular rubber band is topologically equivalent to the hexagonal rubber band as it is related to continuous deformation, and stretching in this case. However, the circular rubber band differs topologically from the figure-eight shape, where the crossing point is joined. When we unglue this point by stretching, it splits into two separate points. With further stretching, these points evolve into two diametrically opposite points on the circle, showing that nearby points lose their neighborhood relationship. Therefore circle and figure eight are topologically non-equivalent; the circle has one hole characterized by genus $(g) = 1$, while figure eight has two holes *i.e.* $g = 2$. In context to the materials, if the smooth deformations such as impurities, the geometry of the system, defects, etc. do not alter underlying properties; called topological materials, a new phase of matter [105, 106]. The new phase of matter is a consequence of symmetry and topology [107]. Topology extends beyond the physical form and geometry of materials, influencing their physical properties, including electronic conduction, spin transport, light transmission, and more [104]. Particularly in the context of the materials; topology refers to the study of the band structure and unique properties of materials arising from the underlying topological properties of the electronic wave function [107]. The Noble Prize in Physics 2016 was awarded

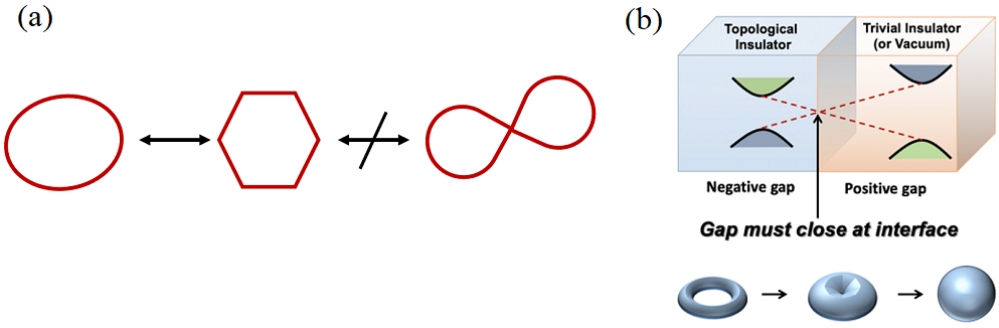

Figure 1.6: (a) Examples of topological equivalence and non-equivalence of different structures. (b) A schematic diagram of the transformation of the trivial insulator to the topological insulator (TI) [104].

'for theoretical discoveries of topological phase transition and topological phases of matter' [108]. A famous example of a topological material is a topological insulator (TI). The band insulator and TI's both have an energy gap; the former has a positive gap while the latter has a negative band gap. Moving from the trivial insulator to the TI, the energy gap must vanish at the interface; at the surface (transition is discontinuous transformation). Therefore, the surface becomes conducting,

while the bulk remains insulating. This example is equivalent to the transformation of the baseball into a donut [Fig. 1.6 (b)]. As long as deformation is 'continuous', the TI possesses the conducting surface state due to its topological protection. Topological materials can be broadly classified into two categories: topological insulators (TIs) [109] and topological semimetals (TSMs) [110].

1.3.1 Topological insulators and Quantum Hall state

Topological insulators (TIs) in two or three dimensions have the insulating energy gap in the bulk while conducting (gapless) edge or surface states at the boundary of the sample [109, 111]. The simplest band diagram of TI is shown in Fig.1.7(a), which shows that the bulk is insulating while conducting surface states residing in the bulk energy gap. These surface states typically display Dirac cone-type dispersion, where spin and momentum are mutually perpendicular and locked [109, 112]. The surface states of TIs arise from the SOC and the protected by $\mathcal{T}$-symmetry. These surface states are robust and maintained even when disorder and defects are present. A 2D TI works as a quantum spin Hall insulator, while in a 3D TI, unique spin-polarized 2D Dirac fermions emerge at its surface [109, 111, 113]. The conducting gapless electronic states exhibit chirality by propagating electrons along the edge in a single direction. These states are unaffected by disorder since there are no available states for backscattering to occur [109]. Figure1.7 (b) illustrates the ordinary in-

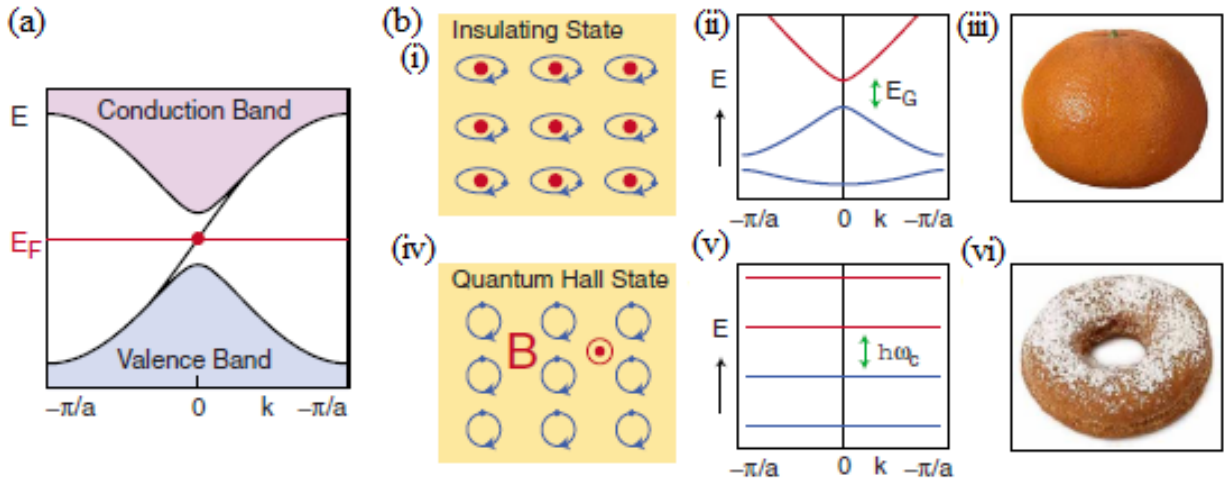

Figure 1.7: (a) A simple band diagram of the topological insulator (TI). (b) State of the matter. (i)-(iii) Representations of insulating state.(i) An atomic representation of an insulator. (ii) An insulating band structure (iii) A sphere without a hole. (iv-vi) Representations of quantum Hall state. (iv) The cyclotron motion of electrons. (v) Landau levels, conceptualized as a band structure. (vi) A donut with one hole [109].

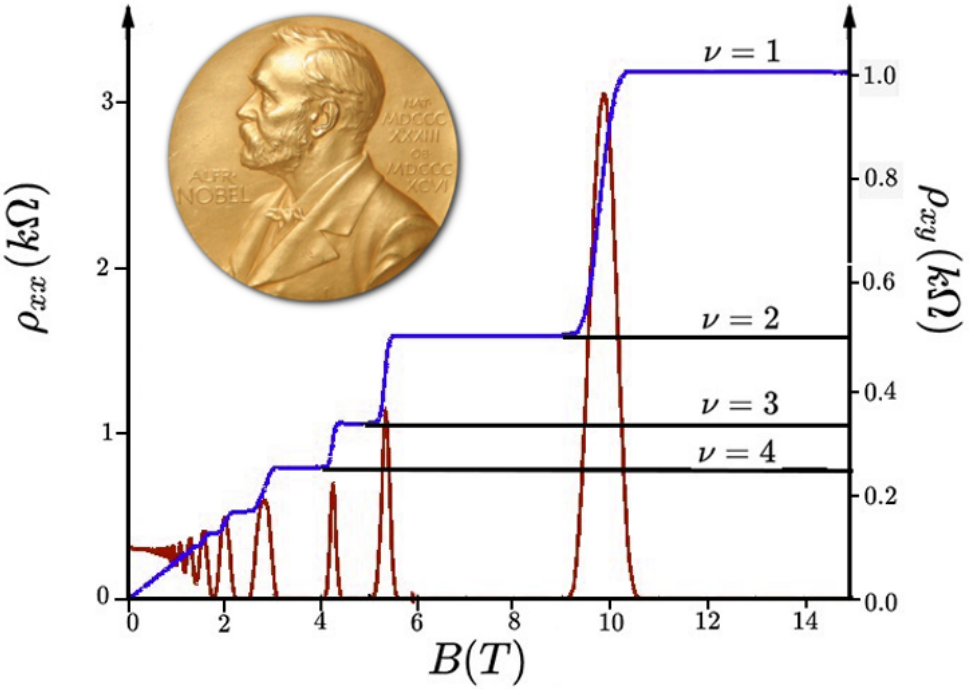

Figure 1.8: (a) The schematic diagram of the longitudinal resistivity (left axis) and quantization of Hall resistance (right axis) in the two-dimensional electron gas [114].

sulator and the quantum Hall insulator states. In conventional insulators, electrons are bound to atoms [Fig.1.7 (b)i] with quantized energy levels, creating an energy gap E_g between occupied and empty bands [Fig.1.7 (b)ii]. In the simplest scenario, distant atoms lead to energy independence from momentum, resulting in localized states and a perfectly flat band [109]. In contrast to this, if the electrons are confined in the 2D-plane under a strong magnetic field, they undergo the cyclotron motion [Fig.1.7 (b)iv] [115]. In the presence of the magnetic field, the x and y components of momentum do not commute. However, introducing a unit cell with area $2\pi\hbar c/eB$ enclosing a quantum of magnetic flux makes the x and y momenta commute, leading to a band structure depicted in [Fig.1.7(b)v] [109]. This band structure looks similar to an insulator energy level but with different energy separation of $\hbar\omega_c$, termed Landau levels [109, 115]. Nevertheless, these two band structures differ significantly. When an electric current is applied within the plane, the cyclotron orbit drifts perpendicularly to the magnetic field, generating an electric current orthogonal to the electric field. As a result, the Hall conductivity becomes quantized to $\frac{ne^2}{h}$ [109, 115]. The phenomenon of quantization of Hall conductivity or resistivity in the 2D electron gas is called the quantum Hall effect (QHE) that originally discovered by Klaus von Klitzing, who received the Nobel Prize in 1985 [109, 115]. A schematic diagram of the longitudinal resistivity (left axis) and quantization

of Hall resistance (right axis) in the 2D electron gas is shown in Fig.1.8. The 2D electron gas is where the electrons are allowed to move in 2-dimensions and tightly bound to the third dimension. Transistor-like structures such as metal–oxide semiconductor devices, field-effect transistors, high-electron-mobility-transistors (HEMTs), and rectangular quantum wells are common examples of 2D electron gases. The fundamental disparity between the insulator and quantum Hall insulator states is a matter of topology. The topological classification of gapped band structures involves considering the equivalence classes of Hamiltonians that can be transformed into one another without closing the energy gap. The analogy of the insulator and quantum Hall insulator state is similar to the sphere with genus =0 [Fig.1.7(b)iii] and a donut with genus=1 [Fig.1.7(b)vi], as they can not be transformed without closing the gap. This classification is based on a topological invariant called the Chern invariant (C) $\in \mathbb{Z}$ ($\mathbb{Z}$ denotes the integers). The Chern invariant is the total Berry flux in the Brillouin zone and can be expressed as [116]

$$C = \frac{1}{2\pi} \int d^2k \, \Omega_n$$

where Ω_n is the Berry curvature. The Chern number remains invariant even in the presence of degeneracies of occupied bands as long as the energy gap remains the same. By using the Kubo formula quantized Hall conductivity was determined as $\sigma_{xy} = Ce^2/h$, which remains invariant when the Hamiltonian varies smoothly [109]. The simplest example of a 2D TI, also called a quantum spin Hall insulator is graphene [111], where the Dirac points are protected by $\mathcal{T}$ and $\mathcal{P}$ symmetries. In the presence of SOC, the Hamiltonian splits into two identical copies for the spin-up and down system, which does not violate $\mathcal{T}$-symmetry breaking as broken $\mathcal{T}$-symmetry flips both spins. In the presence electric field both the spins move in opposite directions, leading to zero quantum Hall effect but non-zero quantized SHE. The quantized spin Hall conductivity was discovered in the HgTe/CdTe quantum well [22, 23]. In 2006, three separate theoretical teams independently found that the way we describe the quantum spin Hall insulator state can naturally extend into three dimensions termed as topological insulators (TIs) demonstrating bulk topological order and conducting surface states [117, 118]. The TIs are characterized by $\mathbb{Z}_2$ topological invariant, which is zero for the weak TIs when the even number of Dirac cones exist on the surface states while strong TIs for the odd number of Dirac cones enclosed by the surface states that result in the Berry phase of π

when moving Dirac cone's edges [109, 119]. The strong TI is robust against disorder and impurities [109]. Owing to the Kramers theorem, a $\mathcal{T}$-invariant perturbation cannot create an insulating gap at the surface's Dirac point. Introducing a $\mathcal{T}$ symmetry-breaking perturbation on the surface can render a TI insulating throughout its bulk and surface [109]. The topological insulating phase was predicted in several materials such as $Bi_{1-x}Sb_x$, strained HgTe, and α-Sn [117]. In 2008 the first topological insulator state was experimentally discovered in the $Bi_{1-x}Sb_x$ [120]. This was followed by the identification of other TIs such as Bi_2Se_3, Bi_2Te_3, and Sb_2Te_3, etc [121]. In the quest for the search of topological materials, a novel class of materials has been unearthed, denoted as topological semimetals (TSMs). The semimetal exhibits a small or vanishing density of states at the Fermi energy [110].

1.3.2 Topological semimetal

Topological semimetals (TSMs) exhibit a small finite density of states at the Fermi energy, resulting from the band crossing or touching of the conduction and valence bands within the 3D Brillouin zone [110]. These crossings generally result in a topological phase transition and are linked with the topological invariant, therefore the materials hosting such types of crossing points are recognized as topological materials [110, 122, 123]. The TSMs can be categorized mainly two distinct categories based on the dimensionality of their band crossings. The first category is zero-dimensional (0D) band crossings, commonly referred to as nodes or nodal points [124]. The well-known examples of 0D crossings are Dirac semimetals (DSMs) and Weyl semimetals (WSMs), wherein two bands, either doubly (for DSMs) or singly degenerate (for WSMs), intersect at specific locations close to the Fermi energy (E_F), which results in the creation of fourfold Dirac points or twofold Weyl points [Fig.1.9 (a)] [125]. The second class of this material is a fourfold or twofold band crossing along 1D in the Brillouin zone known as the nodal line semimetals [126]. Band crossings in TSMs have two main types: accidental and essential. Accidental crossings arise from band inversions in the Brillouin zone and can be removed maintaining the symmetry [122]. Essential crossings are enforced by the symmetry of the space group and cannot be removed while preserving symmetry [122]. Figure1.9 (b) represents the flow chart of various topological states when breaking the symmetries [122]. Considering the band inversion between two bands in red and blue color (Fig.1.9(b))

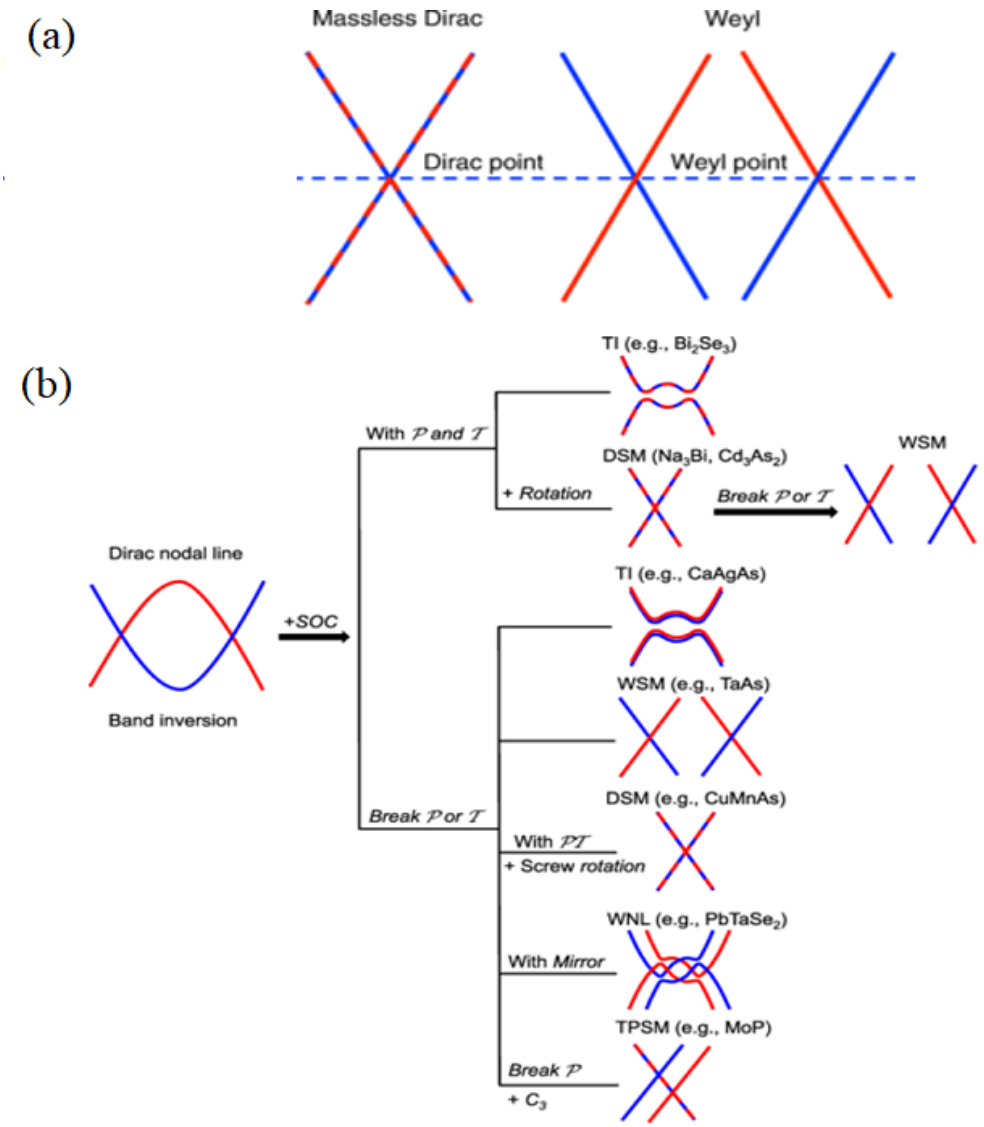

Figure 1.9: (a) The Dirac and Weyl points formed by the linear crossings of fourfold and twofold degenerate bands, respectively. (b) Various topological states induced by band inversion. The mixed color represents the degenerate states while the uniform color is for non-degenerate bands [122].

assuming they are not coupled with SOC and cross each other at certain k points. When turning on the SOC, these bands will transfer in different topological states depending on the strength of the SOC, orbital character, and crystal symmetry [122].

1. If $\mathcal{P}$ and $\mathcal{T}$-symmetries are preserved; the SOC perturbation results in a TI, if the Fermi energy is located within the bulk energy gap. The examples are 3D TI Bi_2Se_3 [121], and PbTe family TI [127], etc. Also if there is an additional symmorphic symmetry for example n-fold uniaxial rotation symmetry, the SOC results in the four-fold 3D DSM as observed in Na_3Bi [123] and Cd_3As_2 [128].

2. If the system has no $\mathcal{P}$ or $\mathcal{T}$-symmetries, the presence of SOC can result in the following topological states;

   (a) In the absence of any additional symmetries that can protect the band crossing, introducing SOC can transform the system into a completely gapped TI state, for example, CaAgAs [129].

   (b) In an appropriate magnitude of SOC, the system can be transformed in a WSMs state with two orthogonal orbital touching at discrete k points and gapped out elsewhere as observed in the TaAs family [130].

   (c) The system with combined $\mathcal{PT}$ symmetry, the spin-degeneracy remains preserved even in the presence of SOC. When an extra crystal symmetry is present for e.g. screw rotational symmetry in CuMnAs, it leads to the emergence of DSM states, where Dirac points are protected by two-fold screw rotation symmetry [131].

   (d) The mirror reflection symmetry in the system protects the nodal line in the absence of SOC. If the system is $\mathcal{PT}$-asymmetric then incorporation of SOC can lead to the two-fold degenerate Weyl nodal line, e.g. in $PbTaSe_2$ [132].

Dirac Semimetal

The Dirac semimetals (DSMs) are characterized by the four-fold Dirac points, resulting from the linear band crossings of two spin-degenerate bands [122]. In the presence of crystal symmetry, the 3D Dirac point can be protected and stabilized [133]. In the DSMs, the electron behaves as zero mass fermions leading to exotic magnetic, optic, and transport properties [134]. The famous examples of the DSMs are Na_3Bi [123], Cd_3As_2 [128], and $PdTe_2$ families [135], etc. Na_3Bi crystallizes in the hexagonal structure with C_3 rotational axis, which is crucial for stabilizing the Dirac point [123]. Figure1.10 shows the band structure of Na_3Bi in the absence and presence of SOC [123]. In the absence of SOC, a band inversion occurs at Γ point. With the inclusion of SOC, the majority of interband crossings between the inverted bands exhibit gaps, excluding the gapless points along the rotational axis *i.e.* Γ-A axis. These crossings involve distinct irreducible representations under C_3 rotational symmetry. With both $\mathcal{T}$ and $\mathcal{P}$ symmetries, each band is spin-degenerate. Consequently,

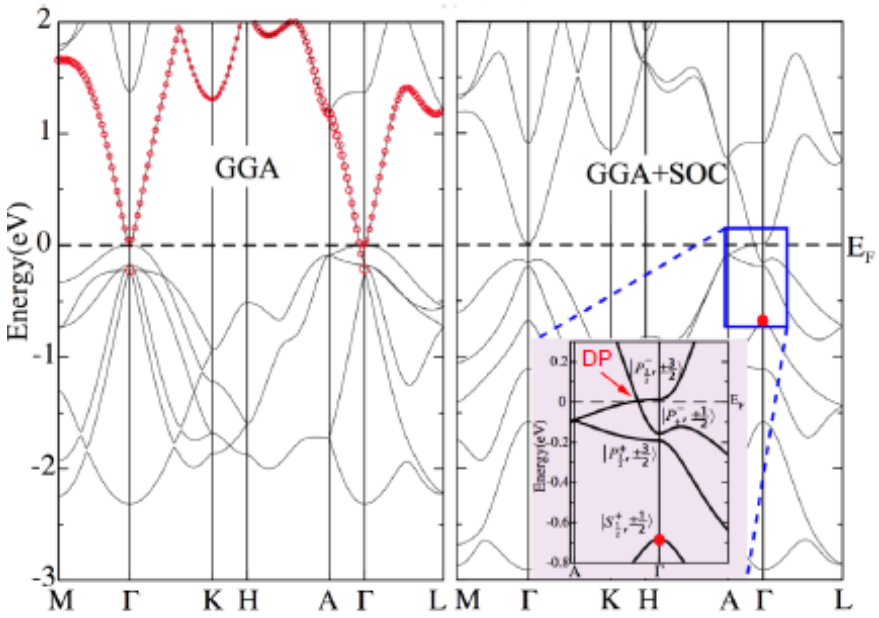

Figure 1.10: (a) Band structure of Na_3Bi in the absence (left) and presence (right) of SOC [123].

band inversion results in two Dirac points along the $\Gamma - A$ direction [123]. Quantum transport measurements play a crucial role in characterizing 3D DSMs. Many intriguing transport phenomena were revealed in 3D DSMs including high carrier mobility and magnetoresistance [136], strong SdH oscillations with a non-trivial π Berry phase [137], planar Hall effect [138], chiral anomaly-induced negative longitudinal magnetoresistance [139], anomalous Hall and Nernst effect [140], etc. The type-II DSMs were discovered, which are marked by strongly tilted Dirac cones in the k-space (e.g. transition-metal dichalcogenides ($PtSe_2$, $PtTe_2$, $PdTe_2$) [141], KMgBi [142] etc. In addition to non-magnetic DSMs preserving the $\mathcal{T}$ and $\mathcal{P}$ symmetries, the magnetic DSMs also exist, when considering the three-dimensional antiferromagnetic system that breaks both $\mathcal{T}$ and $\mathcal{P}$ symmetries but respects the combined $\mathcal{PT}$ symmetries symmetry, therefore satisfying condition $(\mathcal{PT})^2 = -1$, the two-fold degeneracy is preserved, and if there is certain crystal symmetry to protect the degenerate band result into the four-fold Dirac fermions [122]. For example, the antiferromagnetic CuMnAs and CuMnP were predicted to host the Dirac fermion near the Fermi energy [131].

Weyl semimetal

Weyl fermions, initially predicted in high-energy physics have not yet been discovered yet, but they have been found to emerge in the Weyl semimetals (WSMs) upon breaking either $\mathcal{P}$ or $\mathcal{T}$

symmetry in DSMs [143]. Therefore the $\mathcal{P}$-breaking WSMs are nonmagnetic and the $\mathcal{T}$-breaking WSMs are magnetic [143]. For the realization of $\mathcal{P}$-breaking WSMs, different routes have been proposed such as stacking of trivial and topological insulators and phase transition between the trivial to topological insulator in non-centrosymmetric systems, etc. [122]. However experimental evidence for the realization of Weyl fermion in the proposed model is not available, as they require fabrication of heterostructures, precise tuning of SOC, and requirement of pressure. Therefore the natural $\mathcal{P}$-breaking compounds are more feasible to investigate the possible Weyl semimetallic state. Indeed, the TaAs family comprises the first experimentally discovered $\mathcal{P}$-breaking WSMs [130, 144]. The family members of TaAs crystallize in the tetragonal structure (space group $I4_1md$) [144].

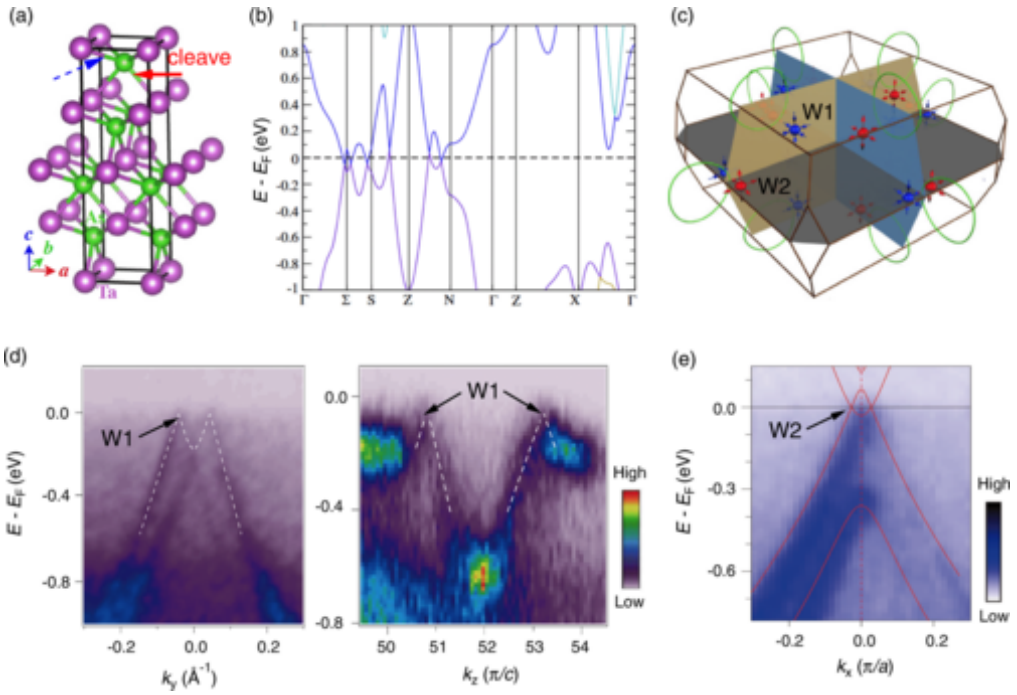

Figure 1.11: (a) TaAs crystal structure. (b) The electronic band structure of TaAs in the absence of SOC. (c) The nodal rings circle and Weyl points in the Brillouin zone. (d) ARPES intensity plot in k_y and k_z directions through a pair of W_1 Weyl nodes. (e) k_x direction proximate to the W_2 Weyl nodes [122, 144–146]

.

TaAs crystal structure comprises alternating layers of As and Ta [Fig.1.11(a)]. The neighboring TaAs layers undergo a 90° rotation and a shift of a/2, resulting in the lack of inversion symmetry. The crystal structure consists of mirror planes m_x and m_y, which protect the band crossings and these crossings form the nodal line on two mirror invariant planes (a detailed discussion of the nodal line is in the next section). The band structure of TaAs is shown in Fig.1.11(b) [144]. With

SOC, nodal lines gap out, and the accidental band touching occurs between valence and conduction bands at discrete *k*-points, forming gapless Weyl points. In particular, there are a total of 12 pairs of Weyl points in the Brillouin zone, each carrying monopole charges of ± 1 [144]. Four pairs (W_2) align precisely in the $k_z = 0$ plane, while another eight pairs (W_1), are situated off the $k_z = 0$ plane as shown in Fig.1.11(c) . It should be noted that the number of Weyl points depends on the symmetry of the system, e.g. two mirror planes m_x and m_y, $\mathcal{T}$-symmetry, and nonsymmorphic C_4 rotation in TaAs gives 24 Weyl points in the entire Brillouin zone [144]. The signature of the Weyl semimetallic state in this family is verified by angle-resolved photoemission spectroscopy (ARPES) as shown in Fig.1.11(d) and (e) [145, 146]. The striking feature of Weyl semimetal is the existence of the Fermi arc [122]. From the first principles calculation and the surface-sensitive VUV ARPES measurements, the fermi arc was found in the TaAs compound and its family members compounds [130]. The quantum transport provides a versatile tool for the investigation of the existence of Weyl point using chiral anomaly *i.e.* the negative longitudinal magnetoresistance when the electric field is applied parallel to the magnetic field, which has been reported in TaAs [147], TaP [148], NbP [149], etc. The continued search for the WSMs reveals a new phase of WSMs through $\mathcal{T}$-breaking known as magnetic WSMs [122, 125]. The magnetic WSMs allow the minimum number of Weyl points *i.e.* two with opposite chirality [150]. Several materials have been proposed as magnetic WSMs such as $HgCr_2Se_4$ [151], magnetic pyrochlores $A_2Ir_2O_7$ (A = rare earth element) [152], $YbMnBi_2$ [153], Heusler compounds [154, 155], antiferromagnetic Mn_3Sn family [156] and $Co_3Sn_2S_2$ [157], antiferromagnetic Half Heusler compound GdPtBi [158] and NdPtBi [143], etc. Recently, ARPES and STS data confirm Weyl semimetal state in $YbMnBi_2$ [153] and $Co_3Sn_2S_2$ [157], revealing surface Fermi arcs and bulk Weyl cones. $Co_3Sn_2S_2$ crystallizes in the rhombohedral space group with the magnetization of Co along c-direction [Fig.1.12 (a)] [159]. Without SOC, multiple band inversions occur, centered at the L point [Fig.1.12 (b)], leading to the formation of several nodal rings at the three mirror planes within the Brillouin zone. Upon the consideration of SOC, these nodal rings gap out, resulting in the emergence of a pair of Weyl points situated 60 meV above the Fermi energy [159]. These Weyl points result in the emergence of pairs of significant Fermi arcs on the (001) surface as shown in Fig.1.12 (c) [160].

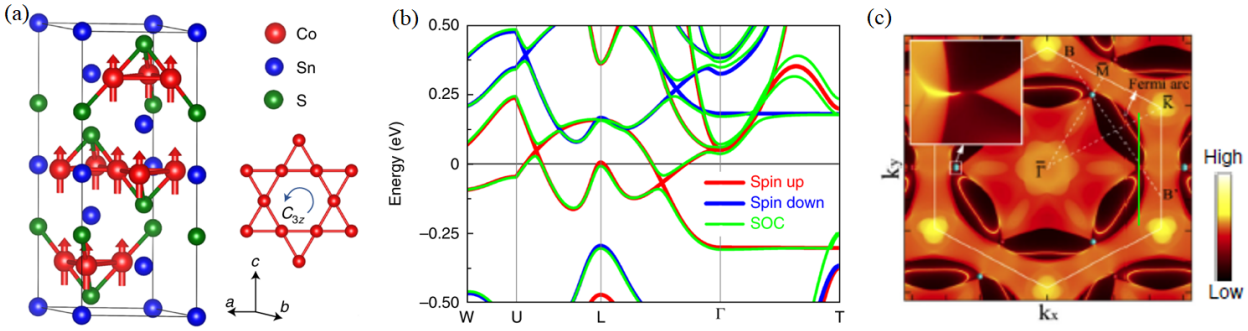

Figure 1.12: (a) Crystal structure of $Co_3Sn_2S_2$, in which the moment of Co is aligned in c-direction. (b) Electronic band structure of $Co_3Sn_2S_2$. (c) Fermi surface of $Co_3Sn_2S_2$ [159, 160].

Topological nodal line semimetal

Besides isolated points, band crossing points in 3D momentum space can also create 1D loops. Materials featuring these near the Fermi level are termed topological nodal-line semimetals (TNLSMs). The TNLSMs exhibit several distinct features [122];

1. TNLSMs exhibit in 1D bulk Fermi in contrast to the DSMs and WSMs having 0 D Fermi surface.

2. Unlike massless Weyl and Dirac cones, 1D nodal lines show linear crossing only perpendicular to the line. This leads to massless excitations in perpendicular direction, while massive along the line.

3. TNLSMs are characterized by nontrivial topological invariant monopole charges. If we consider two points at the two sides of the nodal line then the difference between the number of bands with eigenvalue +1 below the chosen point is 1 then the crossing is protected by mirror reflection symmetry. The topological invariant for mirror symmetry-protected nodal lines is denoted as Z and has a value of 1. Another essential topological invariant is the Berry phase, particularly when considering $\mathcal{PT}$ symmetry, where the Berry phase must exhibit quantization as an integer multiple of π, while another closed loop possesses a Berry phase of zero.

4. Crystallographic symmetries stabilize nodal lines, but these protections do not extend to surfaces. Thus, bulk-edge correspondence does not apply to TNLSMs, and surface states are not topologically protected. Still, TNLSMs have flat “drumhead” surface states within the gap between bands.

Several systems have been identified as TNLSMs. For example in $\mathcal{PT}$-symmetric systems like Cu_3PdN [161], graphene networks [162], and CaTe [163], the nodal lines find stability through band inversion. Mirror symmetry such as mirror reflection and mirror glide can stabilize the nodal line in the systems such as TaAs [144], and Ca_3P_2 [164]. Similar nodal lines have been forecasted in $SrIrO_3$ [165], ZrSiS [166], IrO_2 [167], etc. When the SOC is present, two kinds of nodal line is possible one is the Weyl nodal line, and the other is the Dirac nodal line. For the Weyl nodal line, either $\mathcal{P}$ or $\mathcal{T}$ symmetry must be broken and the examples include the $HgCr_2Se_4$ [168], $Pb(Tl)TaSe_2$ [132], and $InNbS_2$ [169], etc. If the system has both broken $\mathcal{P}$ and $\mathcal{T}$ symmetry *i.e.* $\mathcal{PT}$ symmetric system then in combination with the nonsymmorphic crystal symmetry the Dirac nodal line stabilizes at the Brillouin zone boundary. Dirac nodal lines are expected in various materials, including

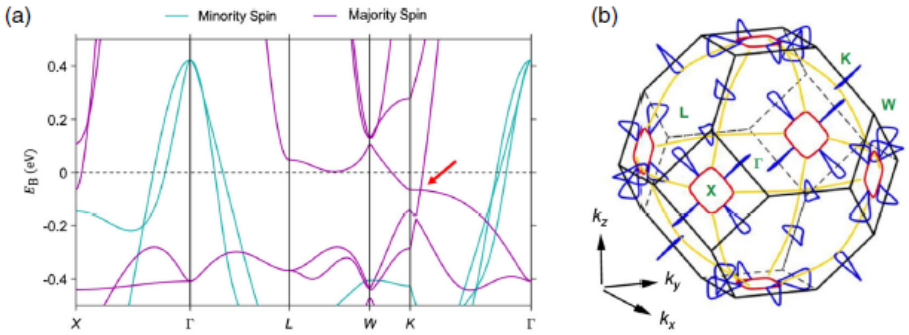

Figure 1.13: (a) Band structure of Co_2MnGa Heusler alloy. (b) The 3-dimensional plot of the Weyl nodal lines in the bulk Brillouin zone of Co_2MnGa [122].

$SrIrO_3$ [165], IrF_4 [170], and InBi [171], etc. belonging to the nonsymmorphic space groups. Another important class of TNLSM is the magnetic nodal line semimetal, based on which we can divide nodal lines into magnetic and non-magnetic nodal line semimetals [122]. Several magnetic nodal-line materials found such as Fe_3GeTe_2 [172], CrO_2, LnX (Ln=La, Gd; X=Cl, Br) [173], and Co_2MnGa which reveals Weyl nodal lines with drumhead surface states [174]. Co_2MnGa is a ferromagnetic compound that exhibits the crossings from majority spin states near the Fermi energy as shown in Fig.1.13 (a) by an arrow. These twofold band crossings form the Weyl nodal line near the Brillouin zone boundary as shown in Fig.1.13 (b) in the red, yellow, and blue colors. It is worthwhile to mention here that besides the 0D and 1D crossings, the third type of crossing is also possible in the 3D Brillouin zone that is preserved on the 2D surface called nodal surface semimetal, however, this class has not been extensively explored [122, 175].

1.3.3 Topological semimetal: Source of Berry curvature

The WSMs and NLSMs are essential materials for large transport response due to the presence of the Weyl points/nodal lines, which give rise to the intriguing physical phenomenon and exceptional electronic properties [176–178]. The Weyl points act as the source and sink of the Berry curvature and hence lead to the sizeable anomalous Hall and Nernst effects, particularly when they are situated near the Fermi energy [177, 179]. The Weyl points/nodal lines are connected with some topological invariant, making the electronic state more effective against the disorder and the impurities [125]. This inherent property translates to highly effective transport capabilities across a longer distance [125]. Consider a two-fold degenerate system, the generic Hamiltonian can be written as [90]

$$H(\vec{k}+\vec{q}) = v\,\vec{q}\cdot\vec{\sigma}$$

where is σ is the Pauli matrix. This is a general 2×2 matrix with the eigenvalue $\pm v$q. The corresponding eigenvector can be written in terms of polar coordinates (θ,ϕ)

$$|u_- >= \begin{bmatrix} e^{-i\phi} sin\theta/2 \\ cos\theta/2 \end{bmatrix} \quad |u_+ >= \begin{bmatrix} e^{-i\phi} cos\theta/2 \\ sin\theta/2 \end{bmatrix}$$

One has the liberty to add any arbitrary phase to these wave functions. For lower energy levels the Berry connection can be given as

$$A_\theta = \langle u_-|i\partial_\theta|u_-\rangle = 0 \quad A_\phi = \langle u_-|i\partial_\phi|u_-\rangle = sin^2\theta/2$$

Berry curvature can be given as [90]

$$\Omega_{\theta\phi} = \partial_\theta A_\phi - \partial_\phi A_\theta = \frac{1}{2} sin\theta \tag{1.23}$$

The $|u_-\rangle$ is undefined at $\theta = \pi$. Therefore if we adopt another gauge and multiply $|u_-\rangle$ by $e^{i\phi}$, the wave function will be smooth and single-valued everywhere excluding $\theta = 0$. In this case $\partial_\theta A_\theta = 0$ and $\partial_\theta A_\phi$ = -$cos^2\theta/2$. However, the Berry curvature which is gauge invariant quantity will be the

same $\frac{1}{2}sin\theta$. Using inverse Jacobian

$$\Omega_{q_iq_j} = \frac{1}{2}\frac{\partial(\theta,\phi)}{\partial(q_iq_j)}$$

the Berry curvature can be written in the set of parametric spaces as follows [90]

$$\vec{\Omega} = \frac{1}{2}\frac{\vec{q}}{q^3} \tag{1.24}$$

It is evident from Eq.1.24 that this Berry curvature is due to the monopole situated at q=0 [180]. Therefore the two-fold degenerate system such as the Weyl points is equivalent to the magnetic monopole and acts as the source and drain of Berry curvature. The integral of Berry curvature from a sphere containing the magnetic monopole, which is the Berry phase on the sphere is [90]

$$\gamma = \int_{s^2} \partial\theta\partial\phi\Omega_{\theta\phi} = 2\pi \tag{1.25}$$

$$C = \frac{\gamma}{2\pi} = 1 \tag{1.26}$$

Typically, the integrated Berry curvature over a closed manifold quantizes in 2π units, representing monopoles inside—called the Chern number. In addition to the Weyl points if the system accompanying the gapped nodal lines gapped out due to the external perturbation such as SOC the large Berry curvature arises in the surrounding area of gapped nodal lines [98, 177, 181]. The Berry curvature is equivalent to the pseudo magnetic field in the momentum space leading to the anomalous transport response [1, 90]. The anomalous transport behavior becomes more pronounced when the Weyl points/nodal line lies in the vicinity of Fermi energy. For example, the $Co_3Sn_2S_2$ compound shows a large AHC of about 1100 S/cm due to the nodal line and Weyl point near the Fermi energy [159]. PrAlGe [182], $YMnBi_2$ [153], and Mn_3Sn [183] etc., have been identified as the magnetic WSMs and exhibit the large AHC. The intrinsic AHE in ferromagnetic materials based on the Berry phase mechanism, does not necessitate a non-zero Chern number for the band. For a band with a Chern number of zero, the local Berry curvature can still be non-zero, leading to a non-zero AHC [90]. Therefore trivial ferromagnet can also give the AHE. For the ferromagnetic materials, the broken $\mathcal{T}$-symmetry with SOC leads to the non-zero AHC in the materials [184]. Ferromag-

netic materials consistently maintain $\mathcal{T}$-symmetry through spin rotation represented as R_s (θ_s,ϕ_s). The combination of R_s and $\mathcal{T}$-symmetry is called effective $\mathcal{T}$-symmetry, which preserves without considering the SOC and leads to the vanishing AHC in ferromagnetic materials. Therefore for the ferromagnetic materials the SOC becomes necessary for the finite AHE [184]. In the case of coplanar antiferromagnetic systems, the SOC also becomes necessary to disrupt the $R_s\mathcal{T}$ symmetry. However, if one spin is oriented out of the plane, the $R_s\mathcal{T}$ symmetry is naturally broken, even without SOC. As a result, non-coplanar spin structures do not depend on SOC for the AHC [184]. In ferromagnetic materials, the Berry curvature is large when two or more bands approach energetically and hybridize due to SOC [185]. If the Fermi level lies between the gap opened by the SOC the AHC reaches its maximum value $\frac{e^2}{2h}$ [1, 186]. Figure 1.14(a) shows a typical two bands split by the SOC and the Berry curvature (Fig. 1.14(b)) shows the large Hall conductivity when the Fermi

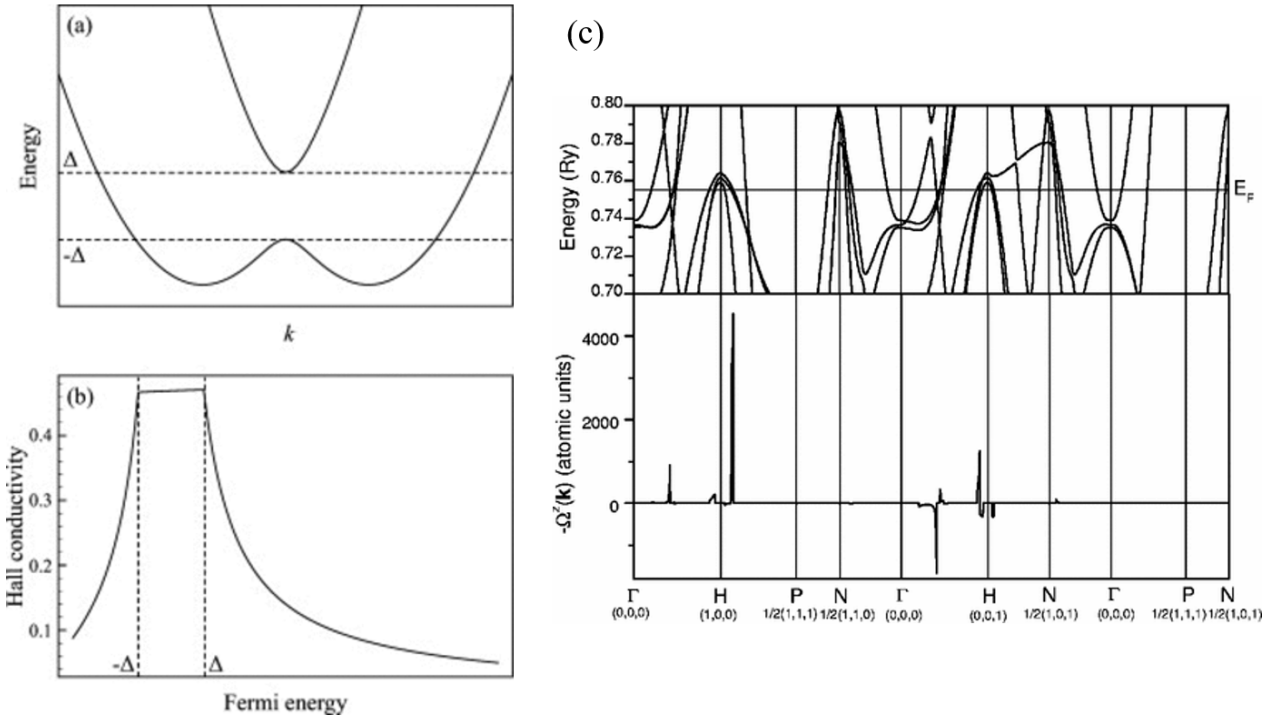

Figure 1.14: (a) Energy dispersion of spin split band. (b) The anomalous Hall conductivity in a unit of $\frac{e^2}{h}$.(c) Band structure and k-resolved Berry curvature for the Fe [187].

level lies in the spin split gap [90]. The Hall conductivity decreases when the Fermi energy moves below or away from the SOC gap. Figure 1.14(c) is the band structure of Fe and the Berry curvature along the same path of the calculated band structure [187]. We can see the band hybridization due to SOC along the H (0,0,0)-P($\frac{1}{2}$,$\frac{1}{2}$,$\frac{1}{2}$) direction. The spikes in Berry curvature arise at the same k

point where the band hybridizes a tiny gap is opened [187]. The large AHC value of about 750 S/cm was calculated in the Fe using the First-principles calculation [187].

1.4 Heusler alloys

The search for advanced materials has been crucial for the progressive realm of materials science and engineering for modern technology. Among these materials, Heusler alloys have emerged as a captivating class of intermetallic systems, exhibiting a unique combination of properties that hold the potential for various technological applications [188, 189]. In 1903 Fritz Heusler discovered Cu_2MnAl Heusler alloy, which is a ferromagnetic material despite no constituent element being ferromagnetic [190]. These alloys have garnered significant attention from researchers worldwide due to their exceptional versatility, encompassing an impressive range of magnetic, electrical, and thermoelectric characteristics [189]. Heusler alloys are categorized into different types based on their crystal structures and constituent elements. The most common categories include full Heusler alloy (X_2YZ), half-Heusler alloy (XYZ), and inverse Heusler alloy ([XZ]YX) [189]. Here X and Y are transition metals and Z is the p-block element. The half-Heusler alloy crystallizes in the cubic space group ($F\bar{4}3m$) and the X atoms occupy the 4d ($\frac{3}{4},\frac{3}{4},\frac{3}{4}$) site, while Y and Z atoms occupy the 4b ($\frac{1}{2},\frac{1}{2},\frac{1}{2}$) and 4a (0, 0, 0) Wyckoff's position, respectively [189]. A unit cell of the half-Heusler alloy is shown in Fig.1.15 (a). The full Heusler alloy [Fig.1.15 (b)] crystallizes in the cubic space group ($Fm\bar{3}m$) and consists of four interpenetrating face-centered Bravice lattices. The X atoms occupy tetrahedral sites with Wyckoff positions 8c ($\frac{3}{4},\frac{3}{4},\frac{3}{4}$) and Y and Z atoms occupy 4b ($\frac{1}{2},\frac{1}{2},\frac{1}{2}$) and 4a (0, 0, 0), respectively [189]. In the inverse Heusler alloy, the X atoms in placed on 4a (0, 0, 0) and 4d ($\frac{3}{4},\frac{3}{4},\frac{3}{4}$), while Y and Z atoms located as 4b ($\frac{1}{2},\frac{1}{2},\frac{1}{2}$) and 4c ($\frac{1}{4},\frac{1}{4},\frac{1}{4}$), respectively [Fig.1.15 (c)]. This often happens when the atomic number of Y element is bigger than the X atom for example in the Mn_2CoSn [191]. The arrangement of atoms within a Heusler alloy can vary based on electronegativity and atomic sizes, leading to different disordered structures. For instance, these structures may include B2, A2, and DO3 configurations. The B2 structure emerges from the even distribution of Y and Z elements, hence the 4a and 4b sites become equivalent leading to the CsCl type structure (Fig.1.15 (d)) in the space group $Pm\bar{3}m$ [189]. In the DO_3 type disorder [Fig.1.15 (e)], the random distribution between the X and Y or X and Z atoms leads to the Fe_3M (M= Al, Ge) type

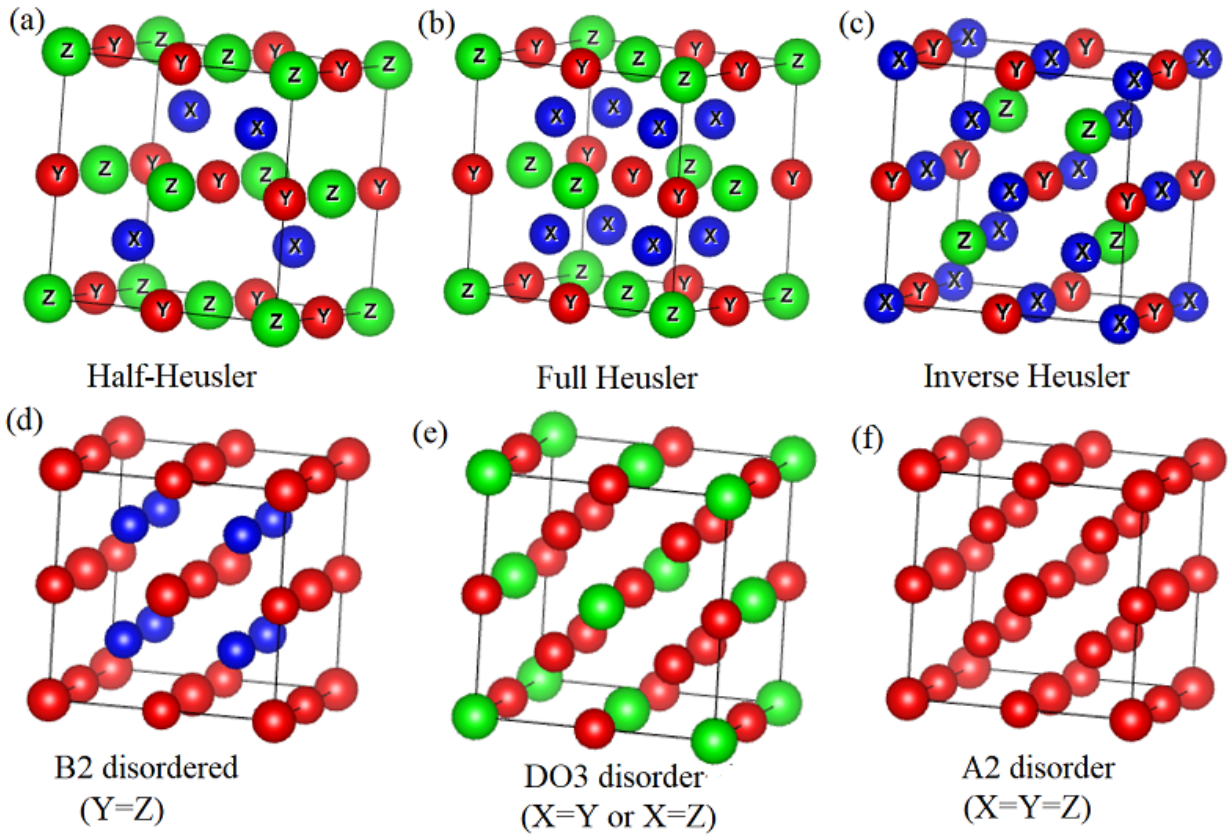

Figure 1.15: Crystal structure of different Heusler alloys (a) Half-Heusler (XYZ) (b) Full-Heusler (X_2YZ). (c) Inverse Heusler ([XZ]YX). (d) B2 type disorder (Y=Z). (e) DO3 disorder (X=Y or X=Z). (f) A2 disorder (X=Y=Z).

structure [192]. In contrast to this partial disorder, some systems show an A2 type of disorder [Fig.1.15 (f)], where all 4a, 4b, 4c, and 4d sites become equivalent due to the mixing of all elements. The magnetic behavior of certain Heusler alloys adheres to the Slater-Pauling rule, which is represented as $m = N_v - 24$, with m denoting the magnetic moment and N_v signifying the count of valence electrons [193]. Consequently, a Heusler alloy with 24 valence electrons will exhibit non-magnetic characteristics. Similarly, the half-Heusler alloys follow the Slater-Pauling rule, expressed as $m = N_v - 18$. For example, the TiCoSb and TiNiSn which have 18 valence electrons are diamagnetic semiconductors [189, 193]. By changing the valence electron these materials can turn into ferromagnetic materials for example VCoSb [189]. The versatility of Heusler alloys stems from their broad range of tunable band gaps, allowing them to manifest as insulators, topological insulators, metals, semimetals, half-metals, semiconductors, spin-gapless semiconductors, and more [194]. These diverse properties pave the way for various technological applications of Heusler alloys [189]. Heusler alloy showing haf-metallic behavior *i.e* a magnetic system with a

finite density of state for one spin channel and zero for the other spin channel is immensely utilized for the spintronics and memory devices application due to the large spin polarization at the Fermi energy [195–197]. The NiMnSb is the first Heusler alloy discovered as the half-metal [198]. The magnetic tunnel junctions (MTJs) devices revolutionize the storage technology, where the metallic sandwiched layer between two ferromagnets is replaced by an insulating layer, which increases the magnetoresistance about 10 times compared to the giant magnetoresistance (GMR) devices [199, 200]. Among the other Heusler alloys, the Co-based Heusler alloys are prominent for their large Curie-temperature (T_c) [201], high spin-polarization [197], and notably the topological properties [155]. Co-based Heusler alloys have garnered attention because of their significant promise as novel electrode materials in spintronic devices. These devices include MTJs, GMR devices, and the facilitation of spin injection from the ferromagnetic layer into the semiconductor [188, 202].

1.4.1 Heusler alloys as topological semimetal: Realization of large anomalous transport response

Many of the Heusler alloys were found as the magnetic Weyl semimetals (WSMs) such as LnPtBi (Ln=Y, Gd, or Nd), Co_2TiX (X=Si, Ge, or Sn) [203], Co_2FeGe [98], Fe_2MnX (X= P, Sb, As) [204], RPtBi (R=Gd or Nd) [205] and more. The advantage of the magnetic WSMs over the $\mathcal{P}$-breaking WSMs is that the magnetic moment can be regulated by an external magnetic field. Therefore, it is easy to control the topological properties by an external magnetic field [206]. The large anomalous Hall effect in the full Heusler compound was observed due to the breaking of nodal lines [179, 204, 207]. The full Heusler alloy is characterized by the presence of three significant mirror planes m_x, m_y, and m_z, which confer distinct protection to three nodal lines located at k_x=0, k_y=0, and k_z=0 planes [204]. When these nodal lines break out due to the SOC, a large Berry curvature arises surrounding the nodal lines. While the gapped nodal lines produce the non-zero Berry curvature, the closed nodal line exhibits a net outward flux of zero [207, 208]. The specific nodal lines that undergo gapping depend on the magnetization direction. For instance, when the magnetization direction is aligned with the [001] direction, the nodal lines in the k_x=0 and k_y=0 planes undergo gapping, while the nodal line perpendicular to the magnetization direction *i.e.*, in the k_z=0 plane remains unaffected by the SOC. The m_x and m_y no longer remain the symmetry

of the plane when considering the magnetization in [001] direction, while m_z remains the symmetry plane since the z-component of spin S_z is left invariant by the z-component of magnetization direction [209]. Conversely, if the magnetization direction is altered to align with the [111] direction, all three nodal lines undergo gapping [155]. The nodal lines become gapped out due to SOC, nevertheless, at some points, the nodal lines refuse to the breakout, and these points qualify as the Weyl points [155]. Therefore the Weyl points can exist only in the plane in which the nodal lines are gapped out. For example, if the magnetization is in the [001] direction, the Weyl points can only exist in the k_x=0 and k_y=0 planes and cannot exist in the k_z=0 plane [177]. In the full Heusler alloy if the nodal lines lie close to the Fermi level and gapped out due to the SOC, a large AHE manifests within the system due to a large Berry at the Fermi surface [177]. It is worthwhile to mention here the Berry curvature due to Weyl points derived from the gapped nodal lines is often small, as sometimes they lie away from the Fermi energy or other Weyl points lie in the constant of the plane [209]. The large AHE and ANE are predicted in the Fe_2MnX (X= P, Sb, As) [204] due to the breaking of the nodal line very close to the Fermi energy. Since the Co-based Heusler alloys have a large Curie temperature, the large anomalous Hall and Nernst effects in these systems would be beneficial for device applications at room temperature as well as at high-temperature [210]. Wang *et al.* thoroughly studied the existence of nodal lines and the Weyl points in the Co_2ZrSn full Heusler system using first-principles calculation [155]. Co_2MnGe Heusler alloy has been predicted to exhibit the multiple Weyl cone in the band structure [211]. Chang *et.al.* analyzed the nodal line and Weyl points in the Co_2TiX (X= Si, Ge or Sn) using the first principles calculation [203]. Recently, a giant AHC of about 1600 S/cm has been observed in the Co_2MnAl ferromagnetic topological semimetal [159]. This large AHE in Co_2MnAl is attributed to the presence of nodal rings and Weyl points near the Fermi energy. Another well-known system is Co_2MnGa Heusler alloy which is reported to show large AHC and ANC about 1200 S/cm and 4.0 A/m-K gue to the gapped nodal lines near the Fermi energy [207]. The large AHE and ANE are theoretically reported in the Co_2FeGe Heusler alloy above 100 meV to the Fermi level due to the SOC-induced nodal line symmetry breaking [98, 212]. Very recently, our group theoretically predicted a large AHC of about 1000 S/cm in the Cu_2CoSn, where the gapping in the nodal line creates large Berry curvature at the Fermi surface [177]. Considering the potential of the Co-based Heusler alloys as the topological

semimetal with large anomalous transport response, high Curie temperature, and high-spin polarization, makes these systems potential candidates for spintronic applications [159, 188, 210]. We are interested in investigating Co-based Heusler alloys, focusing on topological semimetals for large anomalous transport responses. The Berry curvature arising from the topologically protected bands in these materials leads to pronounced anomalous Hall and Nernst effects. The AHE holds potential for spintronics applications, such as nanoscale read head sensors, high-frequency Hall sensors, memory devices, etc. Additionally, the ANE could enable more efficient conversion of heat into electricity compared to traditional thermoelectric materials.

1.5 Objective of present thesis

In this thesis, we aim to investigate Co-based Heusler alloys, with a particular focus on topological semimetals, to explore their potential for exhibiting a large anomalous Hall effect (AHE). The broken time-reversal symmetry in these systems gives non-zero net Berry curvature resulting in unique transport properties such as large AHE, and anomalous Nernst effect (ANE), which is useful for building the spintronic devices [155, 213]. Additionally, Co-based Heusler alloys exhibit high Curie temperature, which makes them ideal for use at room temperature as well as high-temperature [214]. Nonetheless, very few Co-based systems have been studied about AHE, highlighting the need for a deeper understanding of AHE and related topological properties of these materials. Our primary goal is to uncover the intrinsic origin of AHE in these alloys and also identify methods to enhance it. By investigating the electronic structure and magnetic properties of these materials, we aim to correlate these characteristics with their AHE responses. The AHE finds its application in spintronics like magnetic random access memory devices (MRAM) enabling the reading of magnetic states, spin valves, magnetic sensors, highly efficient nanoscale read head sensors, etc. [215–218]. Apart from device applications, AHE is immensely valuable for understanding deeper quantum mechanical behaviors of material, such as spin dynamics, phase transitions, quantum anomalies, magnetic behavior of small devices, spin-orbit and spin-transfer torque-related phenomena, etc. [219–221]. Given the technological potential and fundamental physics of the AHE, we aim to provide a deeper understanding of AHE and topological properties of Co-based Heusler systems by examining the roles of symmetry, disorder, external doping, etc., thereby contributing significantly to the field of

spintronics. Beyond AHE, we also aim to explore new materials with a large anomalous Nernst effect (ANE). The ANE has the potential to convert heat into electricity with better efficiency than conventional thermoelectric materials. Unlike thermoelectricity, where the Peltier effect can occur simultaneously with the Seebeck effect, the ANE generates a voltage in a direction different from the applied temperature gradient, enhancing efficiency. Additionally, we aim to investigate the topological Hall effect and skyrmions in centrosymmetric systems, which have potential applications in race-track memory devices. To conclude, we aim for a deeper scientific understanding of the anomalous transport responses and topological properties of Co-based Heusler alloys, exploring their potential for spintronics and energy harvesting technologies. We employ experimental techniques and theoretical calculations to study the anomalous transport responses of these alloys. The chapter-wise objectives are outlined as follows-

(i). We explored the AHE in the Co_2FeGe Heusler alloy which was theoretically reported to exhibit anomalous Hall conductivity (AHC) of approximately 78 S/cm at the Fermi energy due to the gapped nodal lines [212, 222], however, no experimental details were available. Our goal is to experimentally investigate the AHE in this system and subsequently conduct a theoretical analysis to determine the magnitude of the AHC and identify the source of the Berry curvature.

(ii). Previous research suggests that disorder has a diminishing effect on the AHC within the system [101, 223]. The Co_2FeAl Heusler alloy, which crystallizes into a B2-type disordered structure, provides a platform for exploring the impact of the disorder on the AHE. Additionally, the magnitude of AHC in Co_2FeAl remains controversial across various studies, with experimentally reported values reaching about 100 S/cm, exceeding the theoretically reported AHC of approximately 39 S/cm [214, 224, 225]. Our objective is to investigate AHE in this system and study the influence of disorder on AHE.

(iii). At first, magnetization was thought to be a major factor in the AHE. However, subsequent findings introduced the concept of Berry curvature as the underlying mechanism behind AHE. Co_2MnGa full Heusler alloy is known for its high AHC of approximately 1260 S/cm resulting from Berry curvature associated with gapped nodal lines induced by spin-orbit coupling (SOC) [207]. Our objective is to disrupt the mirror symmetry of Co_2MnGa by substituting one Co atom with its

adjacent Ni atom, thereby keeping the magnetic moment closer to that of Co_2MnGa and study of AHE in the new NiCoMnGa Heusler system to understand the role of Berry curvature.

(iv). Materials with topological nodal lines close to the Fermi energy are crucial for realizing the large anomalous transverse response. The Cu_2CoSn Heusler alloy was predicted as topological semimetal and expected to have a large anomalous Hall response [226]. Our objective is to conduct a systematic theoretical study of AHE and anomalous Nernst effect (ANE) in Cu_2CoSn Heusler system to investigate the topological band feature and origin of large transverse response in this material.

(v). It is widely accepted that non-centrosymmetric materials can host skyrmions due to the DMI resulting from the lattice broken inversion symmetry and significant SOC [227, 228]. While numerous non-centrosymmetric systems have been discovered to host skyrmions, centrosymmetric systems have received limited attention in this context. It is reported in the literature that the thin film heterostructure of Co_2FeAl host skyrmions due to finite DMI originated from the breaking of inversion symmetry and large SOC at the interface. Our objective is to investigate the presence of skyrmions in the bulk centrosymmetric Co_2FeAl, where the role of DMI is disregarded.

It is worth mentioning that by continuing the study of transport properties in time-reversal breaking systems, we expect significant advancement in science and technology. For instance, the discovery of new half-metallic systems with a large anomalous transport response can put forward these materials as promising candidates for spin manipulation and spintronics applications. Half-metals are unique materials where only one spin channel is conductive while the other remains insulating, making them highly advantageous for developing next-generation spintronic devices [229, 230].

References

[1] Naoto Nagaosa, Jairo Sinova, Shigeki Onoda, Allan H MacDonald, and Nai Phuan Ong. Anomalous Hall effect. *Rev. Mod. Phys.*, 82(2):1539, 2010.

[2] Edwin Herbert Hall. On the new action of magnetism on a permanent electric current. *Am. J. Sci.*, 3(117):161–186, 1880.

[3] Edwin Herbert Hall. Xviii. on the "rotational coefficient" in nickel and cobalt. *Lond. Edinb. Dublin philos. mag. j. sci.*, 12(74):157–172, 1881.

[4] A Kundt. On the Hall effect in ferromagnetic materials. *Wied. Ann*, 49:257, 1893.

[5] Alpheus W Smith and RW Sears. The Hall effect in permalloy. *Phys. Rev.*, 34(11):1466, 1929.

[6] Emerson M. Pugh. Hall effect and the magnetic properties of some ferromagnetic materials. *Phys. Rev.*, 36:1503–1511, Nov 1930.

[7] Emerson M Pugh and TW Lippert. Hall emf and intensity of magnetization. *Phys. Rev.*, 42 (5):709, 1932.

[8] Emerson M. Pugh, N. Rostoker, and A. Schindler. On the Hall effect in ferromagnetics. *Phys. Rev.*, 80:688–692, Nov 1950.

[9] Jairo Sinova, Sergio O Valenzuela, Jörg Wunderlich, CH Back, and T Jungwirth. Spin Hall effects. *Rev. Mod. Phys.*, 87(4):1213, 2015.

[10] JE Hirsch. Spin Hall effect. *Phys. Rev. Lett.*, 83(9):1834, 1999.

[11] Axel Hoffmann. Spin Hall effects in metals. *IEEE trans. Magn.*, 49(10):5172–5193, 2013.

[12] Yuichiro K Kato, Roberto C Myers, Arthur C Gossard, and David D Awschalom. Observation of the spin Hall effect in semiconductors. *Sci.*, 306(5703):1910–1913, 2004.

[13] G Mihajlović, JE Pearson, MA Garcia, SD Bader, and A Hoffmann. Negative nonlocal resistance in mesoscopic gold Hall bars: absence of the giant spin Hall effect. *Phys. Rev. Lett.*, 103(16):166601, 2009.

[14] M Morota, Y Niimi, K Ohnishi, DH Wei, T Tanaka, H Kontani, T Kimura, and Y Otani. Indication of intrinsic spin Hall effect in 4d and 5d transition metals. *Phys. Rev. B*, 83(17): 174405, 2011.

[15] Jiyu Fan and Jonghwa Eom. Direct electrical observation of spin Hall effect in Bi film. *Appl. Phys. Lett.*, 92(14), 2008.

[16] K Ando, Saburo Takahashi, K Harii, K Sasage, J Ieda, S Maekawa, and Eiji Saitoh. Electric manipulation of spin relaxation using the spin Hall effect. *Phys. Rev. Lett.*, 101(3):036601, 2008.

[17] Christian Hahn, Grégoire De Loubens, Olivier Klein, Michel Viret, Vladimir V Naletov, and J Ben Youssef. Comparative measurements of inverse spin Hall effects and magnetoresistance in YIG/Pt and YIG/Ta. *Phys. Rev. B*, 87(17):174417, 2013.

[18] Klaus von Klitzing, Tapash Chakraborty, Philip Kim, Vidya Madhavan, Xi Dai, James McIver, Yoshinori Tokura, Lucile Savary, Daria Smirnova, Ana Maria Rey, et al. 40 years of the quantum Hall effect. *Nat. Rev. Phys.*, 2(8):397–401, 2020.

[19] K. v. Klitzing, G. Dorda, and M. Pepper. New method for high-accuracy determination of the fine-structure constant based on quantized Hall resistance. *Phys. Rev. Lett.*, 45:494–497, Aug 1980.

[20] Klaus von Klitzing. Quantum Hall effect: Discovery and application. *Annu. Rev. Condens. Matter Phys.*, 8:13–30, 2017.

[21] Atsufumi Hirohata, Keisuke Yamada, Yoshinobu Nakatani, Ioan-Lucian Prejbeanu, Bernard Diény, Philipp Pirro, and Burkard Hillebrands. Review on spintronics: Principles and device applications. *J. Magn. Magn. Mater.*, 509:166711, 2020.

[22] B Andrei Bernevig and Shou-Cheng Zhang. Quantum spin Hall effect. *Phys. Rev. Lett.*, 96 (10):106802, 2006.

[23] Markus Konig, Steffen Wiedmann, Christoph Brune, Andreas Roth, Hartmut Buhmann, Laurens W Molenkamp, Xiao-Liang Qi, and Shou-Cheng Zhang. Quantum spin Hall insulator state in HgTe quantum wells. *Science*, 318(5851):766–770, 2007.

[24] Chao-Xing Liu, Shou-Cheng Zhang, and Xiao-Liang Qi. The quantum anomalous Hall effect: theory and experiment. *Annu. Rev. Condens. Matter Phys.*, 7:301–321, 2016.

[25] Cui-Zu Chang, Chao-Xing Liu, and Allan H MacDonald. Colloquium: Quantum anomalous Hall effect. *Rev. Mod. Phys.*, 95(1):011002, 2023.

[26] Cui-Zu Chang, Jinsong Zhang, Xiao Feng, Jie Shen, Zuocheng Zhang, Minghua Guo, Kang Li, Yunbo Ou, Pang Wei, Li-Li Wang, et al. Experimental observation of the quantum anomalous Hall effect in a magnetic topological insulator. *Sci.*, 340(6129):167–170, 2013.

[27] Yujun Deng, Yijun Yu, Meng Zhu Shi, Zhongxun Guo, Zihan Xu, Jing Wang, Xian Hui Chen, and Yuanbo Zhang. Quantum anomalous Hall effect in intrinsic magnetic topological insulator $MnBi_2Te_4$. *Sci.*, 367(6480):895–900, 2020.

[28] M Serlin, CL Tschirhart, H Polshyn, Y Zhang, J Zhu, K Watanabe, T Taniguchi, L Balents, and AF Young. Intrinsic quantized anomalous Hall effect in a moiré heterostructure. *Sci.*, 367(6480):900–903, 2020.

[29] Masaki Mizuguchi and Satoru Nakatsuji. Energy-harvesting materials based on the anomalous nernst effect. *STAM*, 20(1):262–275, 2019.

[30] Gerrit EW Bauer, Eiji Saitoh, and Bart J Van Wees. Spin caloritronics. *Nat. Mater.*, 11(5): 391–399, 2012.

[31] Masaki Mizuguchi. Control of anomalous nernst effect in spintronic materials. *Jpn. J. Appl. Phys.*, 57(9):0902A6, 2018.

[32] Han Wang, Yingying Dai, Gan-Moog Chow, and Jingsheng Chen. Topological Hall transport: Materials, mechanisms and potential applications. *Prog. Mater. Sci.*, 130:100971, 2022.

[33] KS Denisov, IV Rozhansky, NS Averkiev, and E Lähderanta. General theory of the topological Hall effect in systems with chiral spin textures. *Phys. Rev. B.*, 98(19):195439, 2018.

[34] G Metalidis and P Bruno. Topological Hall effect studied in simple models. *Phys. Rev. B.*, 74(4):045327, 2006.

[35] Börge Göbel, Alexander Mook, Jürgen Henk, and Ingrid Mertig. Antiferromagnetic skyrmion crystals: Generation, topological Hall, and topological spin Hall effect. *Phys. Rev. B.*, 96(6):060406, 2017.

[36] Börge Göbel, Ingrid Mertig, and Oleg A Tretiakov. Beyond skyrmions: Review and perspectives of alternative magnetic quasiparticles. *Phys. Rep.*, 895:1–28, 2021.

[37] Kenya Ohgushi, Shuichi Murakami, and Naoto Nagaosa. Spin anisotropy and quantum Hall effect in the kagomé lattice: Chiral spin state based on a ferromagnet. *Phys. Rev. B.*, 62(10): R6065, 2000.

[38] P Bruno, VK Dugaev, and M Taillefumier. Topological Hall effect and Berry phase in magnetic nanostructures. *Phys. Rev. Lett.*, 93(9):096806, 2004.

[39] Y Taguchi, Y Oohara, H Yoshizawa, N Nagaosa, and Y Tokura. Spin chirality, Berry phase, and anomalous Hall effect in a frustrated ferromagnet. *Sci.*, 291(5513):2573–2576, 2001.

[40] Y Taguchi, T Sasaki, S Awaji, Y Iwasa, T Tayama, T Sakakibara, S Iguchi, T Ito, and Y Tokura. Magnetic field induced sign reversal of the anomalous Hall effect in a pyrochlore ferromagnet Nd2Mo_2O_7: Evidence for a spin chirality mechanism. *Phys. Rev. Lett.*, 90(25): 257202, 2003.

[41] Toshifumi Taniguchi, Kensuke Yamanaka, Hideya Sumioka, Teruo Yamazaki, Yoshikazu Tabata, and Shuzo Kawarazaki. Direct observation of chiral susceptibility in the canonical spin glass AuFe. *Phys. Rev. Lett.*, 93(24):246605, 2004.

[42] Yoshinori Tokura and Naoya Kanazawa. Magnetic skyrmion materials. *Chem. Rev.*, 121(5): 2857–2897, 2020.

[43] Stefan Heinze, Kirsten Von Bergmann, Matthias Menzel, Jens Brede, André Kubetzka, Roland Wiesendanger, Gustav Bihlmayer, and Stefan Blügel. Spontaneous atomic-scale magnetic skyrmion lattice in two dimensions. *Nat. Phys.*, 7(9):713–718, 2011.

[44] Xichao Zhang, Yan Zhou, Kyung Mee Song, Tae-Eon Park, Jing Xia, Motohiko Ezawa, Xiaoxi Liu, Weisheng Zhao, Guoping Zhao, and Seonghoon Woo. Skyrmion-electronics:

writing, deleting, reading and processing magnetic skyrmions toward spintronic applications. *J. Condens. Matter Phys.*, 32(14):143001, 2020.

[45] Xiuzhen Yu, Yusuke Tokunaga, Yasujiro Taguchi, and Yoshinori Tokura. Variation of topology in magnetic bubbles in a colossal magnetoresistive manganite. *Adv. Mater.*, 29 (3):1603958, 2017.

[46] Ajaya K Nayak, Vivek Kumar, Tianping Ma, Peter Werner, Eckhard Pippel, Roshnee Sahoo, Franoise Damay, Ulrich K Rößler, Claudia Felser, and Stuart SP Parkin. Magnetic antiskyrmions above room temperature in tetragonal Heusler materials. *Nat.*, 548(7669): 561–566, 2017.

[47] Albert Fert, Nicolas Reyren, and Vincent Cros. Magnetic skyrmions: advances in physics and potential applications. *Nat. Rev. Mater.*, 2(7):1–15, 2017.

[48] Sheng Li, Xuewen Wang, and Theo Rasing. Magnetic skyrmions: Basic properties and potential applications. *Interdiscip. Mater.*, 2(2):260–289, 2023.

[49] Shasha Wang, Jin Tang, Weiwei Wang, Lingyao Kong, Mingliang Tian, and Haifeng Du. Electrical detection of magnetic skyrmions. *J. Low Temp. Phys.*, 197:321–336, 2019.

[50] Albert Fert, Vincent Cros, and Joao Sampaio. Skyrmions on the track. *Nat. Nanotechnol*, 8 (3):152–156, 2013.

[51] Naoto Nagaosa and Yoshinori Tokura. Topological properties and dynamics of magnetic skyrmions. *Nat. Nanotechnol*, 8(12):899–911, 2013.

[52] Igor Dzyaloshinsky. A thermodynamic theory of "weak" ferromagnetism of antiferromagnetics. *J. Phys. Chem. Solids*, 4(4):241–255, 1958.

[53] Sebastian Mühlbauer, Benedikt Binz, F Jonietz, Christian Pfleiderer, Achim Rosch, Anja Neubauer, Robert Georgii, and Peter Böni. Skyrmion lattice in a chiral magnet. *Sci.*, 323 (5916):915–919, 2009.

[54] XZ Yu, Yoshinori Onose, Naoya Kanazawa, Joung Hwan Park, JH Han, Yoshio Mat-

sui, Naoto Nagaosa, and Yoshinori Tokura. Real-space observation of a two-dimensional skyrmion crystal. *Nat.*, 465(7300):901–904, 2010.

[55] K Shibata, XZ Yu, T Hara, D Morikawa, N Kanazawa, K Kimoto, S Ishiwata, Y Matsui, and Y Tokura. Towards control of the size and helicity of skyrmions in helimagnetic alloys by spin–orbit coupling. *Nat. Nanotechnol.*, 8(10):723–728, 2013.

[56] B Lebech, J Bernhard, and T Freltoft. Magnetic structures of cubic FeGe studied by small-angle neutron scattering. *J. Condens. Matter Phys.*, 1(35):6105, 1989.

[57] XZ Yu, Naoya Kanazawa, Yoshinori Onose, K Kimoto, WZ Zhang, Shintaro Ishiwata, Yoshio Matsui, and Yoshinori Tokura. Near room-temperature formation of a skyrmion crystal in thin-films of the helimagnet FeGe. *Nat. Mater.*, 10(2):106–109, 2011.

[58] Shinichiro Seki, XZ Yu, S Ishiwata, and Yoshinori Tokura. Observation of skyrmions in a multiferroic material. *Sci.*, 336(6078):198–201, 2012.

[59] T Adams, A Chacon, M Wagner, A Bauer, G Brandl, B Pedersen, H Berger, P Lemmens, and C Pfleiderer. Long-wavelength helimagnetic order and skyrmion lattice phase in Cu_2OSeO_3. *Phys. Rev. Lett.*, 108(23):237204, 2012.

[60] K Karube, K Shibata, JS White, T Koretsune, XZ Yu, Y Tokunaga, HM Rønnow, R Arita, T Arima, Y Tokura, et al. Controlling the helicity of magnetic skyrmions in a β-Mn-type high-temperature chiral magnet. *Phys. Rev. B.*, 98(15):155120, 2018.

[61] Joseph A. M. Paddison, Binod K. Rai, Andrew F. May, Stuart Calder, Matthew B. Stone, Matthias D. Frontzek, and Andrew D. Christianson. Magnetic interactions of the centrosymmetric skyrmion material Gd_2PdSi_3. *Phys. Rev. Lett.*, 129:137202, Sep 2022.

[62] Dola Chakrabartty, Sk Jamaluddin, Subhendu K Manna, and Ajaya K Nayak. Tunable room temperature magnetic skyrmions in centrosymmetric kagome magnet Mn_4Ga_2Sn. *Commun. Phys.*, 5(1):189, 2022.

[63] Bei Ding, Zefang Li, Guizhou Xu, Hang Li, Zhipeng Hou, Enke Liu, Xuekui Xi, Feng Xu, Yuan Yao, and Wenhong Wang. Observation of magnetic skyrmion bubbles in a van der waals ferromagnet Fe_3GeTe_2. *Nano Lett.*, 20(2):868–873, 2019.

[64] Bei Ding, Jie Cui, Guizhou Xu, Zhipeng Hou, Hang Li, Enke Liu, Guangheng Wu, Yuan Yao, and Wenhong Wang. Manipulating spin chirality of magnetic skyrmion bubbles by in-plane reversed magnetic fields in $(Mn_{1-x}Ni_x)_{65}Ga_35$ (x= 0.45) magnet. *Phys. Rev. Appl.*, 12(5):054060, 2019.

[65] Claudia Felser and Stuart Parkin. Topology, skyrmions, and Heusler compounds. *MRS Bulletin*, 47(6):600–608, 2022.

[66] Tsuyoshi Okubo, Sungki Chung, and Hikaru Kawamura. Multiple-q states and the skyrmion lattice of the triangular-lattice heisenberg antiferromagnet under magnetic fields. *Phys. Rev. Lett.*, 108(1):017206, 2012.

[67] Melvin A Ruderman and Charles Kittel. Indirect exchange coupling of nuclear magnetic moments by conduction electrons. *Phys. Rev.*, 96(1):99, 1954.

[68] Takashi Kurumaji, Taro Nakajima, Max Hirschberger, Akiko Kikkawa, Yuichi Yamasaki, Hajime Sagayama, Hironori Nakao, Yasujiro Taguchi, Taka-hisa Arima, and Yoshinori Tokura. Skyrmion lattice with a giant topological Hall effect in a frustrated triangular-lattice magnet. *Sci.*, 365(6456):914–918, 2019.

[69] Max Hirschberger, Taro Nakajima, Shang Gao, Licong Peng, Akiko Kikkawa, Takashi Kurumaji, Markus Kriener, Yuichi Yamasaki, Hajime Sagayama, Hironori Nakao, et al. Skyrmion phase and competing magnetic orders on a breathing kagomé lattice. *Nat. Commun.*, 10(1): 5831, 2019.

[70] Nguyen Duy Khanh, Taro Nakajima, Xiuzhen Yu, Shang Gao, Kiyou Shibata, Max Hirschberger, Yuichi Yamasaki, Hajime Sagayama, Hironori Nakao, Licong Peng, et al. Nanometric square skyrmion lattice in a centrosymmetric tetragonal magnet. *Nat. Nanotechnol.*, 15(6):444–449, 2020.

[71] S Ishiwata, T Nakajima, J-H Kim, DS Inosov, N Kanazawa, JS White, JL Gavilano, R Georgii, KM Seemann, G Brandl, et al. Emergent topological spin structures in the centrosymmetric cubic perovskite $SrFeO_3$. *Phys. Rev. B.*, 101(13):134406, 2020.

[72] James C Loudon, Alison C Twitchett-Harrison, David Cortés-Ortuño, Max T Birch, Luke A

Turnbull, Aleš Štefančič, Feodor Y Ogrin, Erick O Burgos-Parra, Nicholas Bukin, Angus Laurenson, et al. Do images of biskyrmions show type-ii bubbles? *Adv. Mater.*, 31(16): 1806598, 2019.

[73] Charudatta Phatak, Olle Heinonen, Marc De Graef, and Amanda Petford-Long. Nanoscale skyrmions in a nonchiral metallic multiferroic: Ni_2MnGa. *Nano lett.*, 16(7):4141–4148, 2016.

[74] Lingyao Kong, Jin Tang, Weiwei Wang, Yaodong Wu, Jialiang Jiang, Yihao Wang, Junbo Li, Yimin Xiong, Mingliang Tian, and Haifeng Du. Observation of hybrid magnetic skyrmion bubbles in Fe_3Sn_2 nanodisks. *Phys. Rev. B.*, 107(17):174425, 2023.

[75] Markus Altthaler, Erik Lysne, Erik Roede, Lilian Prodan, Vladimir Tsurkan, Mohamed A Kassem, Hiroyuki Nakamura, Stephan Krohns, István Kézsmárki, and Dennis Meier. Magnetic and geometric control of spin textures in the itinerant kagome magnet Fe_3Sn_2. *Phys. Rev. Res.*, 3(4):043191, 2021.

[76] Dmitry Shcherbakov, Petr Stepanov, Shahriar Memaran, Yaxian Wang, Yan Xin, Jiawei Yang, Kaya Wei, Ryan Baumbach, Wenkai Zheng, Kenji Watanabe, et al. Layer-and gate-tunable spin-orbit coupling in a high-mobility few-layer semiconductor. *Sci. Adv.*, 7(5): eabe2892, 2021.

[77] Shun-Qing Shen. Spin transverse force on spin current in an electric field. *Phys. Rev. Lett.*, 95:187203, Oct 2005.

[78] Junsaku Nitta. Spin–orbit interaction and spintronics. *JSAP Review*, 2023:230102, 2023.

[79] Shigeki Onoda, Naoyuki Sugimoto, and Naoto Nagaosa. Intrinsic versus extrinsic anomalous Hall effect in ferromagnets. *Phys. Rev. Lett.*, 97(12):126602, 2006.

[80] J Smit. The spontaneous Hall effect in ferromagnetics i. *Physica*, 21(6-10):877–887, 1955.

[81] A Fert and A Friederich. Skew scattering by rare-earth impurities in silver, gold, and aluminum. *Phys. Rev. B.*, 13(1):397, 1976.

[82] Jun Kondo. Anomalous Hall effect and magnetoresistance of ferromagnetic metals. *Prog. Theor. Phys.*, 27(4):772–792, 1962.

[83] Werner Jellinghaus and Miguel Pedro de Andrés. Influenceß of the neighboring elements of iron on the hall effect of iron-rich mixed crystals. *Ann. Physics*, 462(3-4):189–200, 1961.

[84] Luc Berger. Side-jump mechanism for the Hall effect of ferromagnets. *Phys. Rev. B.*, 2(11): 4559, 1970.

[85] Robert Karplus and JM Luttinger. Hall effect in ferromagnetics. *Phys. Rev.*, 95(5):1154, 1954.

[86] Ganesh Sundaram and Qian Niu. Wave-packet dynamics in slowly perturbed crystals: Gradient corrections and Berry-phase effects. *Phys. Rev. B*, 59(23):14915, 1999.

[87] J. M. Luttinger. Theory of the Hall effect in ferromagnetic substances. *Phys. Rev.*, 112: 739–751, Nov 1958.

[88] NA Sinitsyn. Semiclassical theories of the anomalous Hall effect. *J. Condens. Matter Phys.*, 20(2):023201, 2007.

[89] Josef W Zwanziger, Marianne Koenig, and Alexander Pines. Berry's phase. *Annu. Rev. Phys. Chem.*, 41(1):601–646, 1990.

[90] Di Xiao, Ming-Che Chang, and Qian Niu. Berry phase effects on electronic properties. *Rev. Mod. Phys.*, 82(3):1959, 2010.

[91] M Gradhand, DV Fedorov, Falko Pientka, P Zahn, I Mertig, and BL Györffy. First-principle calculations of the Berry curvature of bloch states for charge and spin transport of electrons. *Journal of Physics: Condensed Matter*, 24(21):213202, 2012.

[92] Shigeki Onoda, Naoyuki Sugimoto, and Naoto Nagaosa. Intrinsic versus extrinsic anomalous hall effect in ferromagnets. *Phys. Rev. Lett.*, 97:126602, Sep 2006.

[93] Jürgen Kötzler and Woosik Gil. Anomalous hall resistivity of cobalt films: Evidence for the intrinsic spin-orbit effect. *Physical Review B*, 72(6):060412, 2005.

[94] A. Fert and O. Jaoul. Left-right asymmetry in the scattering of electrons by magnetic impurities, and a hall effect. *Phys. Rev. Lett.*, 28:303–307, Jan 1972.

[95] Yugui Yao, Leonard Kleinman, A. H. MacDonald, Jairo Sinova, T. Jungwirth, Ding-sheng Wang, Enge Wang, and Qian Niu. First principles calculation of anomalous hall conductivity in ferromagnetic bcc fe. *Phys. Rev. Lett.*, 92:037204, Jan 2004.

[96] P. N. Dheer. Galvanomagnetic effects in iron whiskers. *Phys. Rev.*, 156:637–644, Apr 1967. doi: 10.1103/PhysRev.156.637. URL https://link.aps.org/doi/10.1103/PhysRev.156.637.

[97] Eric Roman, Yuriy Mokrousov, and Ivo Souza. Orientation dependence of the intrinsic anomalous hall effect in hcp cobalt. *Phys. Rev. Lett.*, 103:097203, Aug 2009.

[98] Gaurav K Shukla, Jyotirmoy Sau, Nisha Shahi, Anupam K Singh, Manoranjan Kumar, and Sanjay Singh. Anomalous hall effect from gapped nodal line in the Co_2FeGe Heusler compound. *Phys. Rev. B*, 104(19):195108, 2021.

[99] Yuan Tian, Li Ye, and Xiaofeng Jin. Proper scaling of the anomalous hall effect. *Phys. Rev. Lett.*, 103:087206, Aug 2009.

[100] Y. Sakuraba, K. Hyodo, A. Sakuma, and S. Mitani. Giant anomalous Nernst effect in the $Co_2MnAl_{1-x}Si_x$ Heusler alloy induced by fermi level tuning and atomic ordering. *Phys. Rev. B*, 101:134407, Apr 2020.

[101] Felix Mende, Jonathan Noky, Satya N Guin, Gerhard H Fecher, Kaustuv Manna, Peter Adler, Walter Schnelle, Yan Sun, Chenguang Fu, and Claudia Felser. Large anomalous Hall and Nernst effects in high curie-temperature iron-based heusler compounds. *Adv. Sci.*, 8(17): 2100782, 2021.

[102] Nisha Shahi, Ajit K Jena, Gaurav K Shukla, Vishal Kumar, Shivani Rastogi, KK Dubey, Indu Rajput, Sonali Baral, Archana Lakhani, Seung-Cheol Lee, et al. Antisite disorder and berry curvature driven anomalous Hall effect in the spin gapless semiconducting Mn_2CoAl heusler compound. *Phys. Rev. B*, 106(24):245137, 2022.

[103] Gaurav K Shukla, Ajit K Jena, Nisha Shahi, KK Dubey, Indu Rajput, Sonali Baral, Kavita

Yadav, K Mukherjee, Archana Lakhani, Karel Carva, et al. Atomic disorder and berry phase driven anomalous Hall effect in a Co_2FeAl Heusler compound. *Phys. Rev. B*, 105(3):035124, 2022.

[104] Sanju Gupta and Avadh Saxena. A topological twist on materials science. *MRS Bulletin*, 39 (3):265–279, 2014.

[105] Binghai Yan and Shou-Cheng Zhang. Topological materials. *Rep. Prog. Phys.*, 75(9): 096501, 2012.

[106] B Andrei Bernevig, Claudia Felser, and Haim Beidenkopf. Progress and prospects in magnetic topological materials. *Nat.*, 603(7899):41–51, 2022.

[107] Benjamin J Wieder, Barry Bradlyn, Jennifer Cano, Zhijun Wang, Maia G Vergniory, Luis Elcoro, Alexey A Soluyanov, Claudia Felser, Titus Neupert, Nicolas Regnault, et al. Topological materials discovery from crystal symmetry. *Nat. Rev. Mater.*, 7(3):196–216, 2022.

[108] David J Thouless, F Duncan M Haldane, and J Michael Kosterlitz. The nobel prize in physics 2016. *Current Science*, 111(8):1293, 2016.

[109] M Zahid Hasan and Charles L Kane. Colloquium: topological insulators. *Rev. Mod. Phys.*, 82(4):3045, 2010.

[110] AA Burkov. Topological semimetals. *Nat. Mater.*, 15(11):1145–1148, 2016.

[111] Charles L Kane and Eugene J Mele. Quantum spin hall effect in graphene. *Phys. Rev. Lett.*, 95(22):226801, 2005.

[112] Stephan Rachel. Interacting topological insulators: a review. *Rep. Prog. Phys.*, 81(11): 116501, 2018.

[113] Junji Haruyama. Quantum-spin-Hall phases and 2d topological insulating states in atomically thin layers. *J. Appl. Phys.*, 129(9), 2021.

[114] Quantum hall effect. URL https://en.wikipedia.org/wiki/Quantum_Hall_effect.

[115] K v Klitzing, Gerhard Dorda, and Michael Pepper. New method for high-accuracy determi-

nation of the fine-structure constant based on quantized Hall resistance. *Phys. Rev. Lett.*, 45 (6):494, 1980.

[116] David J Thouless, Mahito Kohmoto, M Peter Nightingale, and Marcel den Nijs. Quantized Hall conductance in a two-dimensional periodic potential. *Phys. Rev. Lett.*, 49(6):405, 1982.

[117] Liang Fu, C. L. Kane, and E. J. Mele. Topological insulators in three dimensions. *Phys. Rev. Lett.*, 98:106803, Mar 2007.

[118] Rahul Roy. Topological phases and the quantum spin Hall effect in three dimensions. *Phys. Rev. B*, 79:195322, May 2009.

[119] Ankita Phutela, Preeti Bhumla, Manjari Jain, and Saswata Bhattacharya. Exploring strong and weak topological states on isostructural substitutions in $TlBiSe_2$. *Sci. Rep.*, 12(1):21970, 2022.

[120] David Hsieh, Dong Qian, Lewis Wray, Yiman Xia, Yew San Hor, Robert Joseph Cava, and M Zahid Hasan. A topological dirac insulator in a quantum spin Hall phase. *Nat.*, 452(7190): 970–974, 2008.

[121] Haijun Zhang, Chao-Xing Liu, Xiao-Liang Qi, Xi Dai, Zhong Fang, and Shou-Cheng Zhang. Topological insulators in Bi_2Se_3, Bi_2Te_3 and Sb_2Te_3 with a single dirac cone on the surface. *Nat. Phys.*, 5(6):438–442, 2009.

[122] BQ Lv, T Qian, and H Ding. Experimental perspective on three-dimensional topological semimetals. *Rev. Mod. Phys.*, 93(2):025002, 2021.

[123] Zhijun Wang, Yan Sun, Xing-Qiu Chen, Cesare Franchini, Gang Xu, Hongming Weng, Xi Dai, and Zhong Fang. Dirac semimetal and topological phase transitions in A_3Bi ($A =$ Na, K, Rb). *Phys. Rev. B*, 85:195320, May 2012.

[124] Xiangang Wan, Ari M. Turner, Ashvin Vishwanath, and Sergey Y. Savrasov. Topological semimetal and fermi-arc surface states in the electronic structure of pyrochlore iridates. *Phys. Rev. B*, 83:205101, May 2011.

[125] NP Armitage, EJ Mele, and Ashvin Vishwanath. Weyl and dirac semimetals in three-dimensional solids. *Rev. Mod. Phys.*, 90(1):015001, 2018.

[126] Chen Fang, Hongming Weng, Xi Dai, and Zhong Fang. Topological nodal line semimetals. *Chin. Phys. B*, 25(11):117106, 2016.

[127] Timothy H Hsieh, Hsin Lin, Junwei Liu, Wenhui Duan, Arun Bansil, and Liang Fu. Topological crystalline insulators in the SnTe material class. *Nat. commun.*, 3(1):982, 2012.

[128] Zhijun Wang, Hongming Weng, Quansheng Wu, Xi Dai, and Zhong Fang. Three-dimensional dirac semimetal and quantum transport in Cd_3As_2. *Phys. Rev. B*, 88:125427, Sep 2013.

[129] Ai Yamakage, Youichi Yamakawa, Yukio Tanaka, and Yoshihiko Okamoto. Line-node dirac semimetal and topological insulating phase in noncentrosymmetric pnictides CaAgX (X= P, As). *J. Phys. Soc. Japan*, 85(1):013708, 2016.

[130] Shin-Ming Huang, Su-Yang Xu, Ilya Belopolski, Chi-Cheng Lee, Guoqing Chang, BaoKai Wang, Nasser Alidoust, Guang Bian, Madhab Neupane, Chenglong Zhang, et al. A Weyl fermion semimetal with surface fermi arcs in the transition metal monopnictide TaAs class. *Nat. Commun.*, 6(1):7373, 2015.

[131] Peizhe Tang, Quan Zhou, Gang Xu, and Shou-Cheng Zhang. Dirac fermions in an antiferromagnetic semimetal. *Nat. Phys.*, 12(12):1100–1104, 2016.

[132] Guang Bian, Tay-Rong Chang, Raman Sankar, Su-Yang Xu, Hao Zheng, Titus Neupert, Ching-Kai Chiu, Shin-Ming Huang, Guoqing Chang, Ilya Belopolski, et al. Topological nodal-line fermions in spin-orbit metal $PbTaSe_2$. *Nat. comm.*, 7(1):10556, 2016.

[133] Steve M Young, Saad Zaheer, Jeffrey CY Teo, Charles L Kane, Eugene J Mele, and Andrew M Rappe. Dirac semimetal in three dimensions. *Phys. Rev. Lett.*, 108(14):140405, 2012.

[134] Matteo Rini. A textbook dirac semimetal. *Physics*, 16:s81, 2023.

[135] Jadupati Nag, Anshu Kataria, Ravi Prakash Singh, Soma Banik, Aftab Alam, and KG Suresh.

Realizing topological states in type-ii dirac semimetal $PdTe_2$: an angle-resolved photoemission and quantum oscillations study. *Bull. Mater. Sci*, 45:1–5, 2022.

[136] Tian Liang, Quinn Gibson, Mazhar N Ali, Minhao Liu, RJ Cava, and NP Ong. Ultrahigh mobility and giant magnetoresistance in the dirac semimetal cd_3as_2. *Nat. Mater.*, 14(3): 280–284, 2015.

[137] L. P. He, X. C. Hong, J. K. Dong, J. Pan, Z. Zhang, J. Zhang, and S. Y. Li. Quantum transport evidence for the three-dimensional dirac semimetal phase in Cd_3As_2. *Phys. Rev. Lett.*, 113: 246402, Dec 2014.

[138] P. Li, C. H. Zhang, J. W. Zhang, Y. Wen, and X. X. Zhang. Giant planar hall effect in the dirac semimetal $ZrTe_{5-\delta}$. *Phys. Rev. B*, 98:121108, Sep 2018.

[139] Jun Xiong, Satya K Kushwaha, Tian Liang, Jason W Krizan, Max Hirschberger, Wudi Wang, Robert Joseph Cava, and Nai Phuan Ong. Evidence for the chiral anomaly in the dirac semimetal Na_3Bi. *Sci.*, 350(6259):413–416, 2015.

[140] Tian Liang, Jingjing Lin, Quinn Gibson, Tong Gao, Max Hirschberger, Minhao Liu, R. J. Cava, and N. P. Ong. Anomalous Nernst effect in the dirac semimetal Cd_3As_2. *Phys. Rev. Lett.*, 118:136601, Mar 2017.

[141] Huaqing Huang, Shuyun Zhou, and Wenhui Duan. Type-ii dirac fermions in the **$PtSe_2$** class of transition metal dichalcogenides. *Phys. Rev. B*, 94:121117, Sep 2016.

[142] DF Liu, LY Wei, CC Le, HY Wang, X Zhang, N Kumar, C Shekhar, NBM Schröter, YW Li, D Pei, et al. Observation of the critical state to multiple-type dirac semimetal phases in KMgBi. *J. Appl. Phys.*, 129(23), 2021.

[143] Binghai Yan and Claudia Felser. Topological materials: Weyl semimetals. *Annu. Rev. Condens. Matter Phys.*, 8:337–354, 2017.

[144] Hongming Weng, Chen Fang, Zhong Fang, B. Andrei Bernevig, and Xi Dai. Weyl semimetal phase in noncentrosymmetric transition-metal monophosphides. *Phys. Rev. X*, 5:011029, Mar 2015.

[145] BQ Lv, N Xu, HM Weng, JZ Ma, P Richard, XC Huang, LX Zhao, GF Chen, CE Matt, F Bisti, et al. Observation of Weyl nodes in TaAs. *Nat. Phys.*, 11(9):724–727, 2015.

[146] Su-Yang Xu, Ilya Belopolski, Nasser Alidoust, Madhab Neupane, Guang Bian, Chenglong Zhang, Raman Sankar, Guoqing Chang, Zhujun Yuan, Chi-Cheng Lee, et al. Discovery of a Weyl fermion semimetal and topological fermi arcs. *Science*, 349(6248):613–617, 2015.

[147] Xiaochun Huang, Lingxiao Zhao, Yujia Long, Peipei Wang, Dong Chen, Zhanhai Yang, Hui Liang, Mianqi Xue, Hongming Weng, Zhong Fang, et al. Observation of the chiral-anomaly-induced negative magnetoresistance in 3d Weyl semimetal TaAs. *Phys. Rev. X*, 5(3):031023, 2015.

[148] Frank Arnold, Chandra Shekhar, Shu-Chun Wu, Yan Sun, Ricardo Donizeth Dos Reis, Nitesh Kumar, Marcel Naumann, Mukkattu O Ajeesh, Marcus Schmidt, Adolfo G Grushin, et al. Negative magnetoresistance without well-defined chirality in the Weyl semimetal TaP. *Nat. commun.*, 7(1):11615, 2016.

[149] Anna Corinna Niemann, Johannes Gooth, Shu-Chun Wu, Svenja Bäßler, Philip Sergelius, Ruben Hühne, Bernd Rellinghaus, Chandra Shekhar, Vicky Süß, Marcus Schmidt, et al. Chiral magnetoresistance in the Weyl semimetal NbP. *Sci. Rep.*, 7(1):43394, 2017.

[150] KM Taddei, L Yin, LD Sanjeewa, Y Li, J Xing, C Dela Cruz, D Phelan, AS Sefat, and DS Parker. Single pair of Weyl nodes in the spin-canted structure of eucd 2 as 2. *Phys. Rev. B.*, 105(14):L140401, 2022.

[151] Gang Xu, Hongming Weng, Zhijun Wang, Xi Dai, and Zhong Fang. Chern semimetal and the quantized anomalous hall effect in $HgCr_2 Se_4$. *Phys. Rev. Lett.*, 107(18):186806, 2011.

[152] Xiangang Wan, Ari M Turner, Ashvin Vishwanath, and Sergey Y Savrasov. Topological semimetal and fermi-arc surface states in the electronic structure of pyrochlore iridates. *Phys. Rev. B.*, 83(20):205101, 2011.

[153] Sergey Borisenko, Daniil Evtushinsky, Quinn Gibson, Alexander Yaresko, Klaus Koepernik, Timur Kim, Mazhar Ali, Jeroen van den Brink, Moritz Hoesch, Alexander Fedorov, et al.

Time-reversal symmetry breaking type-ii Weyl state in $YbMnBi_2$. *Nat. Commun.*, 10(1): 3424, 2019.

[154] Stanislav Chadov, Shu-Chun Wu, Claudia Felser, and Iosif Galanakis. Stability of Weyl points in magnetic half-metallic Heusler compounds. *Phys. Rev. B.*, 96(2):024435, 2017.

[155] Zhijun Wang, MG Vergniory, S Kushwaha, Max Hirschberger, EV Chulkov, A Ernst, Nai Phuan Ong, Robert J Cava, and B Andrei Bernevig. Time-reversal-breaking Weyl fermions in magnetic Heusler alloys. *Phys. Rev. Lett.*, 117(23):236401, 2016.

[156] Hao Yang, Yan Sun, Yang Zhang, Wu-Jun Shi, Stuart SP Parkin, and Binghai Yan. Topological Weyl semimetals in the chiral antiferromagnetic materials Mn_3Ge and Mn_3Sn. *New J. Phys.*, 19(1):015008, 2017.

[157] Noam Morali, Rajib Batabyal, Pranab Kumar Nag, Enke Liu, Qiunan Xu, Yan Sun, Binghai Yan, Claudia Felser, Nurit Avraham, and Haim Beidenkopf. Fermi-arc diversity on surface terminations of the magnetic Weyl semimetal $Co_3Sn_2S_2$. *Science*, 365(6459):1286–1291, 2019.

[158] Max Hirschberger, Satya Kushwaha, Zhijun Wang, Quinn Gibson, Sihang Liang, Carina A Belvin, Bogdan Andrei Bernevig, Robert J Cava, and Nai Phuan Ong. The chiral anomaly and thermopower of Weyl fermions in the half-Heusler GdPtBi. *Nat. Mater.*, 15(11):1161–1165, 2016.

[159] Enke Liu, Yan Sun, Nitesh Kumar, Lukas Muechler, Aili Sun, Lin Jiao, Shuo-Ying Yang, Defa Liu, Aiji Liang, Qiunan Xu, et al. Giant anomalous Hall effect in a ferromagnetic kagome-lattice semimetal. *Nat. Phys*, 14(11):1125–1131, 2018.

[160] Qiunan Xu, Enke Liu, Wujun Shi, Lukas Muechler, Jacob Gayles, Claudia Felser, and Yan Sun. Topological surface fermi arcs in the magnetic Weyl semimetal $Co_3Sn_2S_2$. *Phys. Rev. B*, 97(23):235416, 2018.

[161] Youngkuk Kim, Benjamin J. Wieder, C. L. Kane, and Andrew M. Rappe. Dirac line nodes in inversion-symmetric crystals. *Phys. Rev. Lett.*, 115:036806, Jul 2015.

[162] Hongming Weng, Yunye Liang, Qiunan Xu, Rui Yu, Zhong Fang, Xi Dai, and Yoshiyuki

Kawazoe. Topological node-line semimetal in three-dimensional graphene networks. *Phys. Rev. B*, 92:045108, Jul 2015.

[163] Yongping Du, Feng Tang, Di Wang, Li Sheng, Er-jun Kan, Chun-Gang Duan, Sergey Y Savrasov, and Xiangang Wan. CaTe: a new topological node-line and dirac semimetal. *npj Quantum Mater.*, 2(1):3, 2017.

[164] Lilia S Xie, Leslie M Schoop, Elizabeth M Seibel, Quinn D Gibson, Weiwei Xie, and Robert J Cava. A new form of Ca_3P_2 with a ring of dirac nodes. *Apl Mater.*, 3(8), 2015.

[165] Yige Chen, Yuan-Ming Lu, and Hae-Young Kee. Topological crystalline metal in orthorhombic perovskite iridates. *Nat. Commun.*, 6(1):6593, 2015.

[166] Leslie M Schoop, Mazhar N Ali, Carola Straßer, Andreas Topp, Andrei Varykhalov, Dmitry Marchenko, Viola Duppel, Stuart SP Parkin, Bettina V Lotsch, and Christian R Ast. Dirac cone protected by non-symmorphic symmetry and three-dimensional dirac line node in ZrSiS. *Nat. Commun.*, 7(1):11696, 2016.

[167] Yan Sun, Yang Zhang, Chao-Xing Liu, Claudia Felser, and Binghai Yan. Dirac nodal lines and induced spin hall effect in metallic rutile oxides. *Phys. Rev. B*, 95:235104, Jun 2017.

[168] Gang Xu, Hongming Weng, Zhijun Wang, Xi Dai, and Zhong Fang. Chern semimetal and the quantized anomalous hall effect in $HgCr_2Se_4$. *Phys. Rev. Lett.*, 107:186806, Oct 2011.

[169] Yongping Du, Xiangyan Bo, Di Wang, Er-jun Kan, Chun-Gang Duan, Sergey Y. Savrasov, and Xiangang Wan. Emergence of topological nodal lines and type-ii Weyl nodes in the strong spin-orbit coupling system InNbX_2 (X = S,Se). *Phys. Rev. B*, 96:235152, Dec 2017.

[170] Tomáš Bzdušek, QuanSheng Wu, Andreas Rüegg, Manfred Sigrist, and Alexey A Soluyanov. Nodal-chain metals. *Nat.*, 538(7623):75–78, 2016.

[171] Sandy Adhitia Ekahana, Shu-Chun Wu, Juan Jiang, Kenjiro Okawa, Dharmalingam Prabhakaran, Chan-Cuk Hwang, Sung-Kwan Mo, Takao Sasagawa, Claudia Felser, Binghai Yan, et al. Observation of nodal line in non-symmorphic topological semimetal InBi. *New J. Phys.*, 19(6):065007, 2017.

[172] Kyoo Kim, Junho Seo, Eunwoo Lee, K-T Ko, BS Kim, Bo Gyu Jang, Jong Mok Ok, Jinwon Lee, Youn Jung Jo, Woun Kang, et al. Large anomalous Hall current induced by topological nodal lines in a ferromagnetic van der waals semimetal. *Nat. Mater.*, 17(9):794–799, 2018.

[173] Simin Nie, Hongming Weng, and Fritz B. Prinz. Topological nodal-line semimetals in ferromagnetic rare-earth-metal monohalides. *Phys. Rev. B*, 99:035125, Jan 2019.

[174] Ilya Belopolski, Kaustuv Manna, Daniel S Sanchez, Guoqing Chang, Benedikt Ernst, Jiaxin Yin, Songtian S Zhang, Tyler Cochran, Nana Shumiya, Hao Zheng, et al. Discovery of topological Weyl fermion lines and drumhead surface states in a room temperature magnet. *Sci.*, 365(6459):1278–1281, 2019.

[175] Weikang Wu, Ying Liu, Si Li, Chengyong Zhong, Zhi-Ming Yu, Xian-Lei Sheng, YX Zhao, and Shengyuan A Yang. Nodal surface semimetals: Theory and material realization. *Phys. Rev. B.*, 97(11):115125, 2018.

[176] AA Burkov. Anomalous hall effect in Weyl metals. *Phys. Rev. Lett.*, 113(18):187202, 2014.

[177] Gaurav K Shukla, Ujjawal Modanwal, and Sanjay Singh. Nodal-line symmetry breaking induced colossal anomalous hall and Nernst effects in Cu_2CoSn Heusler compound. *Appl. Phys. Lett.*, 123(5), 2023.

[178] M Zahid Hasan, Guoqing Chang, Ilya Belopolski, Guang Bian, Su-Yang Xu, and Jia-Xin Yin. Weyl, dirac and high-fold chiral fermions in topological quantum matter. *Nat. Rev. Mater.*, 6(9):784–803, 2021.

[179] Peigang Li, Jahyun Koo, Wei Ning, Jinguo Li, Leixin Miao, Lujin Min, Yanglin Zhu, Yu Wang, Nasim Alem, Chao-Xing Liu, et al. Giant room temperature anomalous hall effect and tunable topology in a ferromagnetic topological semimetal Co_2MnAl. *Nat. Commun.*, 11(1):3476, 2020.

[180] Paul Adrien Maurice Dirac. Quantised singularities in the electromagnetic field. *Proc. Math. Phys. Eng.*, 133(821):60–72, 1931.

[181] Ning-Ning Zhao, Kai Liu, and Zhong-Yi Lu. Large anomalous hall effect induced by gapped nodal lines in GdZn and GdCd. *Phys. Rev. B*, 103(20):205104, 2021.

[182] Daniel Destraz, Lakshmi Das, Stepan S Tsirkin, Yang Xu, Titus Neupert, J Chang, A Schilling, Adolfo G Grushin, Joachim Kohlbrecher, Lukas Keller, et al. Magnetism and anomalous transport in the Weyl semimetal PrAlGe: possible route to axial gauge fields. *npj Quantum Mater.*, 5(1):5, 2020.

[183] Satoru Nakatsuji, Naoki Kiyohara, and Tomoya Higo. Large anomalous Hall effect in a non-collinear antiferromagnet at room temperature. *Nat.*, 527(7577):212–215, 2015.

[184] M-T Suzuki, Takashi Koretsune, Masayuki Ochi, and Ryotaro Arita. Cluster multipole theory for anomalous Hall effect in antiferromagnets. *Phys. Rev. B.*, 95(9):094406, 2017.

[185] Ondřej Stejskal, Martin Veis, and Jaroslav Hamrle. The flow of the Berry curvature vector field. *Sci. Rep.*, 12(1):97, 2022.

[186] Shigeki Onoda, Naoyuki Sugimoto, and Naoto Nagaosa. Quantum transport theory of anomalous electric, thermoelectric, and thermal Hall effects in ferromagnets. *Phys. Rev. B*, 77:165103, Apr 2008.

[187] Yugui Yao, Leonard Kleinman, AH MacDonald, Jairo Sinova, T Jungwirth, Ding-sheng Wang, Enge Wang, and Qian Niu. First principles calculation of anomalous hall conductivity in ferromagnetic bcc Fe. *Phys. Rev. Lett.*, 92(3):037204, 2004.

[188] Kelvin Elphick, William Frost, Marjan Samiepour, Takahide Kubota, Koki Takanashi, Hiroaki Sukegawa, Seiji Mitani, and Atsufumi Hirohata. Heusler alloys for spintronic devices: review on recent development and future perspectives. *STAM*, 22(1):235–271, 2021.

[189] Tanja Graf, Claudia Felser, and Stuart SP Parkin. Simple rules for the understanding of Heusler compounds. *Progress in solid state chemistry*, 39(1):1–50, 2011.

[190] VV Marchenkov and V Yu Irkhin. Half-metallic ferromagnets, spin gapless semiconductors, and topological semimetals based on Heusler alloys: Theory and experiment. *Phys. Met. Metallogr.*, 122:1133–1157, 2021.

[191] Jürgen Winterlik, Gerhard H Fecher, Benjamin Balke, Tanja Graf, Vajiheh Alijani, Vadim Ksenofontov, Catherine A Jenkins, Olga Meshcheriakova, Claudia Felser, Guodong Liu,

et al. Electronic, magnetic, and structural properties of the ferrimagnet Mn_2CoSn. *Phys. Rev. B.*, 83(17):174448, 2011.

[192] Aytac Erkisi and Gokhan Surucu. The investigation do3-type Fe_3M (M= Al, Ga, Si and Ge) full-heusler alloys within first principles study. *Politeknik Dergisi*, 21(4):927–936, 2018.

[193] Sergey V Faleev, Yari Ferrante, Jaewoo Jeong, Mahesh G Samant, Barbara Jones, and Stuart SP Parkin. Unified explanation of chemical ordering, the slater-pauling rule, and half-metallicity in full Heusler compounds. *Phys. Rev. B.*, 95(4):045140, 2017.

[194] Sheron Tavares, Kesong Yang, and Marc A Meyers. Heusler alloys: Past, properties, new alloys, and prospects. *Prog. Mater. Sci.*, page 101017, 2022.

[195] Atsufumi Hirohata, James Sagar, Leonardo Lari, Luke R Fleet, and Vlado K Lazarov. Heusler-alloy films for spintronic devices. *Appl. Phys. A*, 111:423–430, 2013.

[196] Yuya Sakuraba, Jun Nakata, Mikihiko Oogane, Hitoshi Kubota, Yasuo Ando, Akimasa Sakuma, and Terunobu Miyazaki. Huge spin-polarization of l21-ordered co2mnsi epitaxial Heusler alloy film. *Jpn. J. Appl. Phys.*, 44(8L):L1100, 2005.

[197] Jen-Chuan Tung and Guang-Yu Guo. High spin polarization of the anomalous hall current in Co-based Heusler compounds. *New J. Phys.*, 15(3):033014, 2013.

[198] D Orgassa, H Fujiwara, TC Schulthess, and WH Butler. First-principles calculation of the effect of atomic disorder on the electronic structure of the half-metallic ferromagnet nimnsb. *Phys. Rev. B.*, 60(19):13237, 1999.

[199] Stuart Parkin, Xin Jiang, Christian Kaiser, Alex Panchula, Kevin Roche, and Mahesh Samant. Magnetically engineered spintronic sensors and memory. *Proc. IEEE*, 91(5):661–680, 2003.

[200] Sarah M Thompson. The discovery, development and future of gmr: The nobel prize 2007. *J. Phys. D: Appl. Phys.*, 41(9):093001, 2008.

[201] Gerhard H Fecher, Hem C Kandpal, Sabine Wurmehl, Claudia Felser, and Gerd Schönhense. Slater-pauling rule and curie temperature of co2-based Heusler compounds. *J. Appl. Phys.*, 99(8), 2006.

[202] Kohei Hamaya and Michihiro Yamada. Semiconductor spintronics with Co_2-Heusler compounds. *MRS Bulletin*, 47(6):584–592, 2022.

[203] Guoqing Chang, Su-Yang Xu, Hao Zheng, Bahadur Singh, Chuang-Han Hsu, Guang Bian, Nasser Alidoust, Ilya Belopolski, Daniel S Sanchez, Songtian Zhang, et al. Room-temperature magnetic topological Weyl fermion and nodal line semimetal states in half-metallic Heusler Co_2TiX (X= Si, Ge, or Sn). *Sci. Rep.*, 6(1):38839, 2016.

[204] Jonathan Noky, Qiunan Xu, Claudia Felser, and Yan Sun. Large anomalous Hall and Nernst effects from nodal line symmetry breaking in Fe_2MnX (X= P, As, Sb). *Phys. Rev. B.*, 99(16): 165117, 2019.

[205] Chandra Shekhar, Nitesh Kumar, V Grinenko, Sanjay Singh, R Sarkar, H Luetkens, Shu-Chun Wu, Yang Zhang, Alexander C Komarek, Erik Kampert, et al. Anomalous hall effect in Weyl semimetal half-Heusler compounds RPtBi (R = Gd and Nd). *PNAS*, 115(37): 9140–9144, 2018.

[206] Payal Chaudhary, Krishna Kant Dubey, Gaurav K Shukla, Sanjay Singh, Surasree Sadhukhan, Sudipta Kanungo, Ajit K Jena, S-C Lee, S Bhattacharjee, Jan Minár, et al. Role of chemical disorder in tuning the Weyl points in vanadium doped Co_2TiSn. *Phys Rev Mater.*, 5(12):124201, 2021.

[207] Satya N Guin, Kaustuv Manna, Jonathan Noky, Sarah J Watzman, Chenguang Fu, Nitesh Kumar, Walter Schnelle, Chandra Shekhar, Yan Sun, Johannes Gooth, et al. Anomalous Nernst effect beyond the magnetization scaling relation in the ferromagnetic Heusler compound Co_2MnGa. *NPG Asia Materials*, 11(1):16, 2019.

[208] Kaustuv Manna, Yan Sun, Lukas Muechler, Jürgen Kübler, and Claudia Felser. Heusler, Weyl and Berry. *Nat. Rev. Mater.*, 3(8):244–256, 2018.

[209] Benedikt Ernst, Roshnee Sahoo, Yan Sun, Jayita Nayak, Lukas Muechler, Ajaya K Nayak, Nitesh Kumar, Jacob Gayles, Anastasios Markou, Gerhard H Fecher, et al. Anomalous Hall effect and the role of Berry curvature in Co_2TiSn Heusler films. *Phys. Rev. B.*, 100(5): 054445, 2019.

[210] J Kübler, GH Fecher, and C Felser. Understanding the trend in the curie temperatures of Co_2-based Heusler compounds: Ab initio calculations. *Phys. Rev. B.*, 76(2):024414, 2007.

[211] Takashi Kono, Masaaki Kakoki, Tomoki Yoshikawa, Xiaoxiao Wang, Kazuki Goto, Takayuki Muro, Rie Y Umetsu, and Akio Kimura. Visualizing half-metallic bulk band structure with multiple Weyl cones of the Heusler ferromagnet. *Phys. Rev. Lett.*, 125(21):216403, 2020.

[212] Jonathan Noky, Johannes Gooth, Claudia Felser, and Yan Sun. Characterization of topological band structures away from the fermi level by the anomalous Nernst effect. *Phys. Rev. B.*, 98(24):241106, 2018.

[213] Jinyu Zou, Zhuoran He, and Gang Xu. The study of magnetic topological semimetals by first principles calculations. *npj Comput. Mater.*, 5(1):96, 2019.

[214] Hung-Lung Huang, Jen-Chuan Tung, and Guang-Yu Guo. Anomalous Hall effect and current spin polarization in Co_2FeX Heusler compounds (X= Al, Ga, In, Si, Ge, and Sn): A systematic ab initio study. *Phys. Rev. B*, 91(13):134409, 2015.

[215] Abhijit Ghosh, Kevin Garello, Can Onur Avci, Mihai Gabureac, and Pietro Gambardella. Interface-enhanced spin-orbit torques and current-induced magnetization switching of Pd/Co/AlO_x layers. *Phys. Rev. Appl.*, 7(1):014004, 2017.

[216] Ajaya K Nayak, Julia Erika Fischer, Yan Sun, Binghai Yan, Julie Karel, Alexander C Komarek, Chandra Shekhar, Nitesh Kumar, Walter Schnelle, Jürgen Kübler, et al. Large anomalous Hall effect driven by a nonvanishing berry curvature in the noncolinear antiferromagnet Mn_3Ge. *Sci. Adv.*, 2(4):e1501870, 2016.

[217] Menglu Yang, Yuanjing Qu, Tao He, Xiong He, Yunli Xu, Lizhi Yi, Liqing Pan, and Guangduo Lu. Study on anomalous hall effect and spin-orbit torque effect of TbCo-based multilayer films. *Nanomaterials*, 14(9):801, 2024.

[218] Tomoya Nakatani, Prabhanjan D Kulkarni, Hirofumi Suto, Keisuke Masuda, Hitoshi Iwasaki, and Yuya Sakuraba. Perspective on nanoscale magnetic sensors using giant anoma-

lous Hall effect in topological magnetic materials for read head application in magnetic recording. *Appl. Phys. Lett.*, 124(7), 2024.

[219] Minh-Hai Nguyen and Chi-Feng Pai. Spin–orbit torque characterization in a nutshell. *APL Mater.*, 9(3), 2021.

[220] H Ohno, a D Chiba, a F Matsukura, T Omiya, E Abe, T Dietl, Y Ohno, and K Ohtani. Electric-field control of ferromagnetism. *Nat.*, 408(6815):944–946, 2000.

[221] Hang Chen, Xiaolong Fan, Hengan Zhou, Wenxi Wang, YS Gui, C-M Hu, and Desheng Xue. Spin rectification enabled by anomalous Hall effect. *J. Appl. Phys.*, 113(17), 2013.

[222] Jonathan Noky, Yang Zhang, Johannes Gooth, Claudia Felser, and Yan Sun. Giant anomalous Hall and Nernst effect in magnetic cubic heusler compounds. *Npj Comput. Mater.*, 6 (1):77, 2020.

[223] Y Sakuraba, K Hyodo, A Sakuma, and S Mitani. Giant anomalous Nernst effect in the $Co_2MnAl_{1-x}Si_x$ heusler alloy induced by fermi level tuning and atomic ordering. *Phys. Rev. B*, 101(13):134407, 2020.

[224] Sajid Husain, Ankit Kumar, Serkan Akansel, Peter Svedlindh, and Sujeet Chaudhary. Anomalous Hall effect in ion-beam sputtered Co_2FeAl full Heusler alloy thin films. *J. Magn.Magn. Mater.*, 442:288–294, 2017.

[225] Xiaotian Wang, Yueqing Li, Yin Du, Xuefang Dai, Guodong Liu, Enke Liu, Zhongyuan Liu, Wenhong Wang, and Guangheng Wu. Structural, magnetic and transport properties of Co_2FeAl Heusler films with varying thickness. *J. Magn.Magn. Mater.*, 362:52–57, 2014.

[226] Yimin Ji, Wenxu Zhang, Hongbin Zhang, and Wanli Zhang. Spin Hall conductivity and anomalous Hall conductivity in full Heusler compounds. *New J. Phys.*, 24(5):053027, 2022.

[227] Sajid Husain, Naveen Sisodia, Avinash Kumar Chaurasiya, Ankit Kumar, Jitendra Pal Singh, Brajesh S Yadav, Serkan Akansel, Keun Hwa Chae, Anjan Barman, PK Muduli, et al. Observation of skyrmions at room temperature in Co_2FeAl heusler alloy ultrathin film heterostructures. *Sci. Rep.*, 9(1):1085, 2019.

[228] Sougata Mallick, Sujit Panigrahy, Gajanan Pradhan, and Stanislas Rohart. Current-induced nucleation and motion of skyrmions in zero magnetic field. *Phys. Rev. Appl.*, 18(6):064072, 2022.

[229] Takahide Kubota, Sumito Tsunegi, Mikihiko Oogane, Shigemi Mizukami, Terunobu Miyazaki, Hiroshi Naganuma, and Yasuo Ando. Half-metallicity and gilbert damping constant in $Co_2Fe_xMn_{1-x}Si$ Heusler alloys depending on the film composition. *Appl. Phys. Lett.*, 94(12), 2009.

[230] M Shaughnessy, Ryan Snow, L Damewood, CY Fong, et al. Memory and spin injection devices involving half metals. *J. Nanomater.*, 2011, 2011.